Astronomy & Astrophysics

The EDIBLES survey

III. C$_2$-DIBs and their profiles

M. Elyajouri[1], R. Lallement[1], N. L. J. Cox[2], J. Cami[3,4], M. A. Cordiner[5,6], J. V. Smoker[7], A. Fahrang[3,8],
P. J. Sarre[9], and H. Linnartz[10]

[1] GEPI, Observatoire de Paris, PSL University, CNRS, Place Jules Janssen, 92190 Meudon, France
     e-mail: meriem.el-yajouri@obspm.fr
[2] ACRI-ST, 260 route du Pin Montard, 06904 Sophia Antipolis, France
[3] Department of Physics and Astronomy and Centre for Planetary Science and Exploration (CPSX), The University of Western
     Ontario, London, ON N6A 3K7, Canada
[4] SETI Institute, 189 Bernardo Avenue, Suite 100, Mountain View, CA 94043, USA
[5] NASA Goddard Space Flight Center, 8800 Greenbelt Road, Greenbelt, MD 20771, USA
[6] Department of Physics, Catholic University of America, Washington, DC 20064, USA
[7] European Southern Observatory, Alonso de Cordova 3107 Vitacura, Santiago, Chile
[8] School of Astronomy, Institute for Research in Fundamental Sciences, 19395-5531 Tehran, Iran
[9] School of Chemistry, The University of Nottingham, University Park, Nottingham NG7 2RD, UK
[10] Sackler Laboratory for Astrophysics, Leiden Observatory, Leiden University, PO Box 9513, 2300 RA Leiden, The Netherlands

ABSTRACT

Context. An unambiguous identification of the carriers of the diffuse interstellar bands (DIBs) would provide important clues to the life cycle of interstellar matter. The so-called C$_2$-DIBs are a class of very weak bands that fall in the blue part of the optical spectrum and are associated with high column densities of the C$_2$ molecule. DIB profile structures constrain potential molecular carriers, but their measurement requires high signal-to-noise, high-resolution spectra and the use of sightlines without Doppler splitting, as typical for a single-cloud situation.
Aims. Spectra from the ESO Diffuse Interstellar Bands Large Exploration Survey (EDIBLES) conducted at the Very Large Telescope (ESO/Paranal) were explored to identify single-cloud and high C$_2$ column sightlines, extract the corresponding C$_2$-DIBs and study their strengths and profiles, and to investigate in detail any sub-structures.
Methods. The target selection was made based on profile-fitting of the 3303 and 5895 Å Na I doublets and the detection of C$_2$ lines. The C$_2$ (2–0) (8750–8849 Å) Phillips system was fitted using a physical model of the host cloud. C$_2$ column densities, temperatures as well as gas densities were derived for each sightline.
Results. Eighteen known C$_2$-DIBs and eight strong non-C$_2$ DIBs were extracted towards eight targets, comprising seven single-cloud and one multi-cloud line-of-sights. Correlational studies revealed a tight association of the former group with the C$_2$ columns, whereas the non-C$_2$ DIBs are primarily correlated with reddening. We report three new weak diffuse band candidates at 4737.5, 5547.4, and 5769.8 Å. We show for the first time that at least 14 C$_2$-DIBs exhibit spectral sub-structures which are consistent with unresolved rotational branches of molecular carriers. The variability of their peak separations among the bands for a given sightline implies that their carriers are different molecules with quite different sizes. We also illustrate how profiles of the same DIB vary among targets and as a function of physical parameters, and provide tables defining the sub-structures to be compared with future models and experimental results.

Key words. line: profiles – ISM: clouds – ISM: molecules

1. Introduction

Diffuse interstellar bands (DIBs) are over 400 broad spectroscopic absorption features observed in stellar spectra in ultraviolet (UV), visible, and infra-red (IR) ranges (see Sarre 2006, and references therein). Many of the DIB carriers are thought to be large carbonaceous molecules in the gaseous phase, but except for the very likely identification of C$_{60}^+$ (Campbell et al. 2015; Cordiner et al. 2017; Spieler et al. 2017; Walker et al. 2017; Lallement et al. 2018), none of these bands has been definitely assigned to any given species. Identifying the DIB carriers and measuring their response to physical conditions and chemical compositions of interstellar clouds is of high importance. This would add to our rather limited knowledge of the molecular

inventory of these clouds in which small molecules, like C3 (Schmidt et al. 2014) were long the largest species identified. It also would be key to understanding the life cycle of cosmic dust and carbonaceous compounds from dying star ejected envelopes to the birth places of new stars and planetary systems. In this respect, a sub-class of DIBs, the so-called C$_2$-DIBs, is particularly interesting because they are detected in interstellar clouds that are characterized by high columns of the C$_2$ molecule (Thorburn et al. 2003; Galazutdinov et al. 2006; Kaźmierczak et al. 2014), i.e., environments more closely chemically related to the cool, dense molecular clouds where stars form, as opposed to the more diffuse, warmer clouds that pervade the Galaxy.

Sub-structures in DIB profiles are indicative of the molecular structure of carriers and open the way to comparisons

with laboratory spectra. However, such measurements require high-performance spectrographs and to date their use has been restricted to relatively strong DIBs and a limited number of sightlines. In fact, disentangling the spectral components requires high spectral resolution, and, furthermore, is restricted to target stars for with only a small Doppler broadening along the line-of-sight – the so-called single-cloud situation- to avoid blends and sub-structures arising from nearly overlapping bands in different clouds. Most of the strong and narrow optical DIBs have been found to have asymmetric profiles, and in the case of the strongest ones such as DIBs 5797 and 6614 Å (Sarre et al. 1995; Ehrenfreund & Foing 1996; Galazutdinov et al. 2002), 5850, 6234, and 6270 Å (e.g., Krełowski & Schmidt 1997; Galazutdinov et al. 2002), 6376, 6379, and 6196 Å (Walker et al. 2001), sub-structures have been clearly identified which may be consistent with unresolved rotational branch structures associated with electronic transitions of gas-phase molecules. Profiles of several C_2-DIBs and some other weak DIBs have been examined also by Galazutdinov et al. (2002) and Słyk et al. (2006). Asymmetries were found, but in the case of the weak C_2-DIBs these were only seen for the 4963, 5418, 5512, 5541, and 5546 Å bands. Distinct sub-structures were found towards HD 147889 for the 4734, 5175, 5418, 5512, 5546, and 6729, Å DIBs by Galazutdinov et al. (2008).

In the case of the C_2-DIBs, the study of their profiles is particularly difficult. The weakness of the absorption requires a very high signal-to-noise ratio (S/N), a careful correction of telluric lines and disentangling from weak stellar features. In addition, because they are narrow (~0.5 Å), the single-cloud condition[1] is even more stringent. Very high resolution spectra commonly reveal that an apparent single absorption can actually be decomposed into absorptions in several closely related clouds, reflecting the quasi-fractal nature of the dense interstellar matter (Welty & Hobbs 2001). However, the clumps are generally fragments of the same complex, and often share a common environment and consequently possess very similar physical properties. Sightlines with high C_2 columns are crossing a cloud core with a density $\gtrsim 100\,\text{cm}^{-3}$ (higher than the typical diffuse interstellar medium; ISM). It is a relatively rare situation, and therefore, the probability of crossing two independent cloud cores with identical radial velocities and with interstellar columns on the same order is low, i.e., C_2 sightlines with a single absorption offer a good probability of being dominated by a single structure. Detecting and studying the C_2-DIBs is one of the goals of the ESO/VLT EDIBLES survey. EDIBLES is devoted to a deep analysis of the DIB properties and is particularly suited for the study of weak DIBs and their sub-structures, thanks to the high resolution of the UVES spectrograph, and, especially, thanks to the high S/N (Cox et al. 2017). In addition, the large spectral coverage allows the simultaneous study of many gaseous absorption lines across the entire blue to the near-infrared range, like OH_+ that can be used as tracer for the cosmic ray ionization rate (Bacalla et al. 2018).

Here, we present an analysis of individual C_2-DIBs in EDIBLES spectra recorded along seven single-cloud and one multi-cloud lines-of-sight. We additionally show the results of a technique allowing to better reveal spectral sub-structures, namely, the stacking of spectra of different target stars after they have been Doppler shifted to the cloud reference frame. Stacking spectra to enhance the S/N of band profiles has proved to be efficient to reveal DIBs (see, e.g., Lan et al. 2015), however, this is the first use of stacking in a search for profile sub-structures. In doing so, we have examined other absorption bands that may correspond to so far unreported C_2-DIBs.

In Sect. 2, we describe the observations, the telluric line removal, and the selection of single-cloud observations. In Sect. 3, we describe the selection of the C_2 sightlines and the analysis of the C_2 lines. Section 4 presents the selected spectra in the intervening cloud frame, in the spectral regions of the C_2-DIBs classified by Thorburn et al. (2003). We also show the spectral regions containing our potentially new C_2-DIBs. In Sect. 5, we list the wavenumber intervals between the observed absorption sub-peaks, when measurable, and study their variability among the bands. In Sect. 6, we present our optimal profiles obtained by co-addition of the spectra of three targets that have relatively deep DIBs and very similar kinetic temperatures and show how these vary as a function of the kinetic temperature derived from the C_2 analysis. We compare the profiles of each C_2-DIB towards several targets characterized by different C_2 excitation temperatures in Sect. 7. Finally, several correlational studies are presented in Sect. 8. They reveal a distinction between C_2 and non-C_2 DIBs. We discuss the various results in Sect. 9.

2. Observations and single-cloud target selection

2.1. EDIBLES data

EDIBLES observations and data reductions are described in detail in Cox et al. (2017). The S/N values for most sightlines are 400–1000 in the red part, 300–400 in the UV, and ≥ 300 in the near-IR. Two additional data treatments are necessary to realize the goals aimed for in this study.

First, we have corrected all individual exposures recorded with the 564-nm setting (including both the Red Upper and Red Lower detectors) for their telluric lines. The method follows the first of the two procedures described in Cox et al. (2017). It is appropriate for moderately weak lines and uses TAPAS synthetic spectra adapted to the observing site and season (Bertaux et al. 2014). In addition to the telluric correction of the entire spectra, we have used the same method to remove the weak telluric lines that contaminate the spectral region comprising the C_2 Phillips system. During the correction process, we noticed an additional system of narrow telluric lines in the 5780–5815 Å region that are lacking in the present TAPAS model. These very weak lines have been added very recently to the HITRAN database and correspond to the $b^1\Sigma_g^+$ $(v = 3)$–$X^3\Sigma_g^-$ $(v = 0)$ band of O_2 (Gordon et al. 2017). Pending their introduction into TAPAS, we have used a weakly reddened star and extracted the system of lines in this spectral area. We have used this empirical transmittance in the same way as the TAPAS one.

Second, we have stacked the individual multiple exposures of the same target, using the original spectra or the telluric-corrected spectra if necessary. The spectra were Doppler-corrected and interpolated to produce a single spectrum in the heliocentric frame. The spectra obtained with the different instrumental configurations have been concatenated. For overlapping spectral intervals we have not averaged the data; instead we have chosen the data obtained with the grating configuration providing the best S/N, i.e., the 437 nm setting was selected in the 346/437 nm overlap region, and the 560 nm-RedL was selected in the 564 nm-RedL/564 nm-RedU overlap region.

---

[1] Note that the term single-cloud does not necessarily imply the existence of a unique homogeneous cloud but rather, a very narrow velocity dispersion of matter along the line-of-sight (much less than the instrumental resolution).
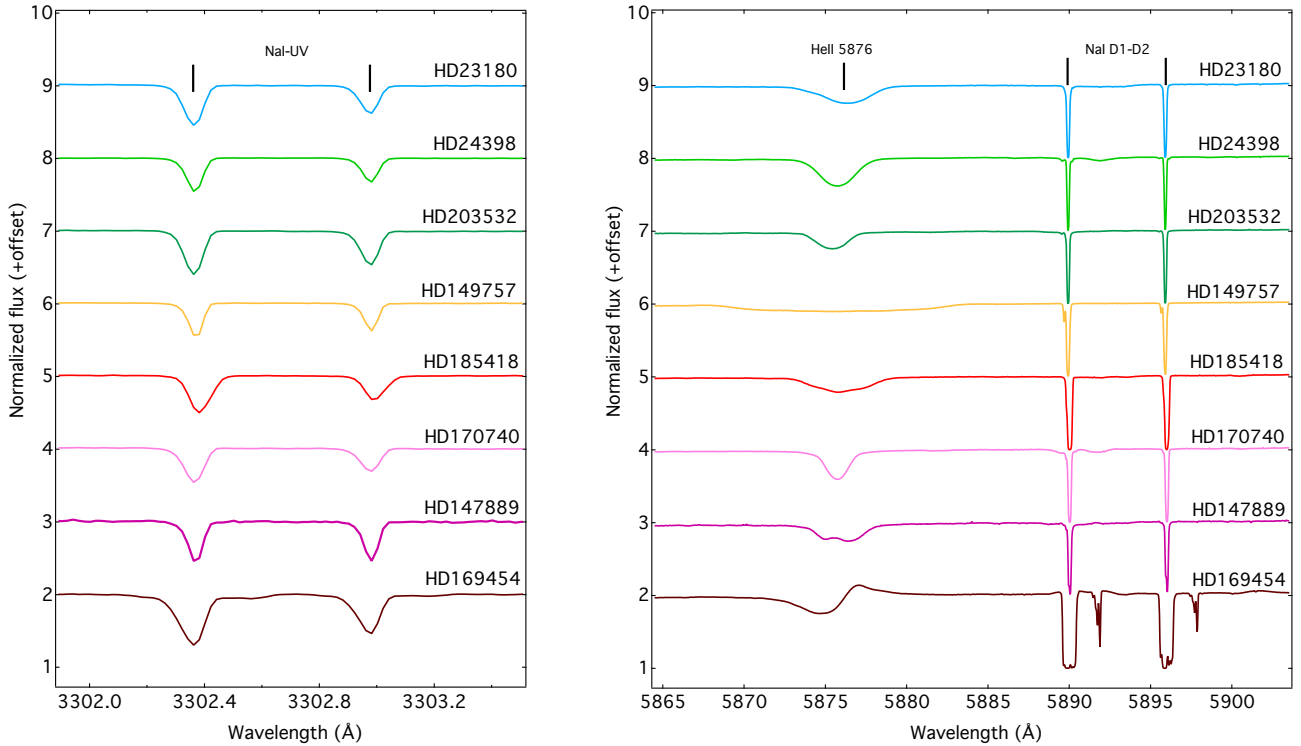
Fig. 1. Na I doublet at 3302.368/3202.987 Å (*left panel*), and Na I D1-D2 and the stellar He II (*right panel*) line are shown for the seven selected single-cloud line-of-sight (one main cloud component) and the multi-cloud target HD 169454. The Na I spectra have been shifted to their air rest wavelengths. The same velocity shift has been applied to the Na I D1-D2 lines. The applied color coding is used in all other figures as well.

2.2. Single-cloud sample selection

Highly reddened lines-of-sight typically intersect more than one interstellar cloud (Welty & Hobbs 2001). Consequently, the resulting DIBs then represent some ill-defined average of the DIB properties along line-of-sight conditions, which complicates the interpretation. In the case of sub-structure studies, the existence of clouds at various radial velocities has the effect of smoothing and suppressing the structures. Therefore, we restrict our study of the C_2-DIBs to single-cloud sightlines, characterized by small Doppler broadening in atomic lines.

In order to select single-cloud sightlines, we have fitted the Na I 3302.368/3202.987 Å UV doublet and the Na I 5890/5896 Å D2-D1 doublet. Due to the intrinsic weakness of the transitions for the UV doublet, there is no or very little saturation and it is easy to determine the number of intervening interstellar clouds with gas columns large enough to produce detectable DIBs. In the case of the 5890/5896 Å doublet there is a strong saturation and line broadening for clouds with C_2, precluding a clear component separation. These transitions have been used to check the structure deduced from the UV doublet. We modeled the absorption lines of the doublets as convolved products of Voigt profiles in combination with a polynomial continuum, and we determined the radial velocities of the major components (see, e.g., Puspitarini & Lallement 2012). Here the shape of the continuum and the number of clouds are determined in a new and totally automated way. To do so, the noise standard deviation is initially measured in regions adjacent to the sodium lines. Model adjustments are then made iteratively for an increasing number of clouds until the residuals in the sodium area become equivalent to the standard deviation. The prior radial velocity of each additional cloud is derived from the location of the minimum in the residuals from the previous step of adjustment.

All spectra and fit results were inspected visually to confirm the presence or absence of multiple velocity components. Figure 1 shows the lack of Doppler splitting in the interstellar Na I lines for the single-cloud selected lines-of-sight which also have detectable C_2 transitions and are subsequently kept in the present study. The selected EDIBLES target stars that satisfy all conditions are: HD 24398, HD 203532, HD 149757, HD 185418, HD 170740, and HD 147889. Note that, in the case of HD 23180, Welty & Hobbs (2001) have found two distinct K I lines at $R \sim 600\,000$, at variance with HD 24398 and HD 149757 that show only one component at the same resolution. However, we keep HD 23180 in the analysis since the Doppler splitting is very low and we assume that the two velocity components belong to two clumps of the same cloud. Table 1 lists their spectral type, radial velocity, and rotation velocity as well as the line-of-sight reddening $E(B–V)$, the total-to-selective extinction ratio R_V, the molecular H_2 fraction $f(H_2)$, and the heliocentric radial velocity of the dominant absorbing cloud. Note that we also added to Fig. 1, to Table 1, and to our study the target star HD 169454. As shown in Fig. 1, this line-of-sight does not represent a single-cloud situation, instead there are two main clouds with radial velocities differing by $\simeq 5$ km s^{-1}, and many more other smaller clouds. We have kept this target for comparison, and also because it is characterized by high reddening $E(B–V)$, strong C_2 lines and deep diffuse bands.

3. Interstellar C_2 lines: detection and analysis

As stated above, the second requirement for our target sample is that they additionally possess detectable C_2 lines. All combined spectra have been visually inspected for the presence of the C_2 (1–0), (2–0), and (3–0) Phillips bands. This requirement greatly reduces the number of appropriate sightlines. Figure 2

Table 1. Single-cloud lines-of-sight properties.

Star						ISM		
Identifier	Spectral type	$v \sin(i)$ (km s^{-1})	$E(B-V)^a$ (mag)	R_V	Ref $R_V{}^b$	f(H$_2$)^c	Na I-UV velocity (km s^{-1})	5797/5780^d
HD 23180	B1 III	100	0.28	3.11	V04	0.51	13.8 ± 0.3	0.73 (ζ)
HD 24398	B1 Ib	43	0.29	2.63	W03	0.60	14.2 ± 0.2	0.53 (ζ)
HD 203532	B3 IV	–	0.30	3.37	V04	0.84	15.2 ± 0.2	0.48 (ζ)
HD 149757	O9.2 IVnn	303	0.32	2.55	V04	0.63	-14.2 ± 0.5	0.43 (ζ)
HD 185418	B0.5 IIIn	–	0.42	2.54	V04	0.40	-10.7 ± 0.5	0.30 (σ)
HD 170740	B2 V	25	0.45	3.01	V04	0.58	-9.9 ± 1.5	0.26 (σ)
HD 147889	B2 V	100	1.03	3.95	V04	0.62	-6.7 ± 1.0	0.41 (ζ)
HD 169454^e	B1 Ia	49	1.03	3.37	V04	–	-9.9 ± 1.5	0.34 (σ)

Notes. $^{(a)}E(B-V)$ is based on photometry and intrinsic colors. $^{(b)}$From Valencic et al. (2004; V04) and Wegner (2003; W03). $^{(c)}$From Jenkins (2009). $^{(d)}$The 5797/5780 DIB ratio is related to the effective UV radiation field strength; UV exposed environments, σ-type, have ratios <0.35, while UV-shielded, ζ-type environments, have ratios ≥0.35 (c.f. Vos et al. 2011). $^{(e)}$HD 169454 is not a single-cloud line-of-sight but it is used for comparison (c.f. Sect. 7).

shows the (2–0) C$_2$ Phillips lines for the resulting sample. The (2–0) band has been chosen for further analysis due to its high oscillator strength, lack of contamination and apparent absence of CCD fringing residuals that adversely affect analysis of the (1–0) band.

Column densities for C$_2$ were derived using a custom fitting procedure written in Python. The (2–0) spectra in the range 8750–8785 Å were normalized to remove the stellar continuum, and the C$_2$ spectrum was fitted using a model consisting of Gaussian absorption profiles characterized by a single Doppler shift (v) and broadening parameter (b), convolved with the 2.8 km s^{-1} UVES point spread function. The model opacity spectrum was generated as a function of column density (N), kinetic temperature ($T_{\rm kin}$) and H + H$_2$ number density (n) using the excitation model of van Dishoeck & Black (1982). Tabulated level populations were obtained from McCall's C$_2$ Calculator^2 (see also Snow & McCall 2006) on a finely sampled T, n grid. Transition wavelengths and oscillator strengths were taken from Sonnentrucker et al. (2007). The set of variable model parameters (v, b, N, T, n), defined in Table 2, was optimized using Levenberg–Marquardt χ^2 minimization until the best fit to the observed spectrum was obtained. The resulting parameter values for each sightline are given in Table 2, and the best-fitting spectral models are shown in Fig. 2. A complete description of all the EDIBLES C$_2$ spectra and their properties will be presented in a separate study (Cordiner et al., in prep.). Parameter uncertainties ($\pm 1\sigma$) were generated using Monte Carlo noise resampling with 200 replications.

4. Extractions of the C$_2$-DIBs

4.1. Extraction of individual C$_2$-DIBs

We have analyzed the spectral regions that correspond to the series of 18 DIBs classified as C$_2$-DIBs by Thorburn et al. (2003), using the DIB wavelength centers listed in this work. For each sightline and each DIB, we have fitted a third order polynomial continuum around the DIB, normalized the spectrum based on this continuum, then determined the DIB equivalent width (EW) as the area between the spectrum and the normalized continuum. Figures 3–7 show the normalized spectra around each C$_2$-DIB for the seven single-cloud targets and HD 169454. These figures also show our choice of the spectral areas on both sides

of the band used for continuum-fitting as well as for the spectral interval used for the EW measurements. As stated in the introduction, it is essential here to identify weak and narrow overlapping stellar lines. In lieu of observing additional, lightly reddened stars of similar spectral types to be used as spectral standards, we used the eight targets together and the fact that stellar line widths must correlate with the rotations (at variance with DIBs). To do so, we have used the full spectrum to estimate the rotational broadening for each target. We also used the rotation velocities $v \sin(i)$ listed in Table 1 when available from the CDS-Simbad website. For example, visual inspection of the stellar He II 5876 Å line in Fig. 1 shows that HD 149757 and HD 185418 are fast rotators while HD 23180, HD 24398, HD 203532, and HD 170740 have narrower photospheric lines; in these latter cases, we checked even more carefully for the presence of narrow stellar lines in the DIB spectral regions that could mimic DIBs or DIB sub-structures (see the cases of 4727, 4963, 5541, 5546, 5762, 6729; Table 3 from Słyk et al. 2006). In the case of the 4734, 5170, 5175, and 6729 Å DIBs, we found that the continuum is contaminated by stellar lines that fall just outside the DIB and, as shown in Figs. 3–7 these lines have been excluded from the fitted spectral interval during the continuum-fitting. In the case of the 4727 Å DIB, it has a double structure suggestive of a blend with a stellar feature on its red side. However, the width of this structure appears to be independent of the stellar rotation. Rather, its shape is perfectly correlated with the main absorption. Therefore, we concluded that this absorption is part of the DIB or an additional, blended DIB, and we measured the total equivalent width of both structures, as shown in Fig. 3. The situation for the 5003 Å DIB is quite different. There we find a blend with an additional absorption, however, this absorption is absent in three other sightlines. We conclude that this feature must be of stellar origin and we keep only the three clean bands.

We used the residuals of continuum fitting to estimate the standard deviation in each DIB spectral interval and for each target. This standard deviation was used in a Monte Carlo noise resampling with 100 replications and we estimated in this way the uncertainty on each DIB EW. All EWs and their uncertainties are listed in Table 3. In exactly the same way, we measured the EWs and associated uncertainties for eight strong non-C$_2$ DIBs, and the results are also listed in Table 3. Their EWs are used in Sect. 8.
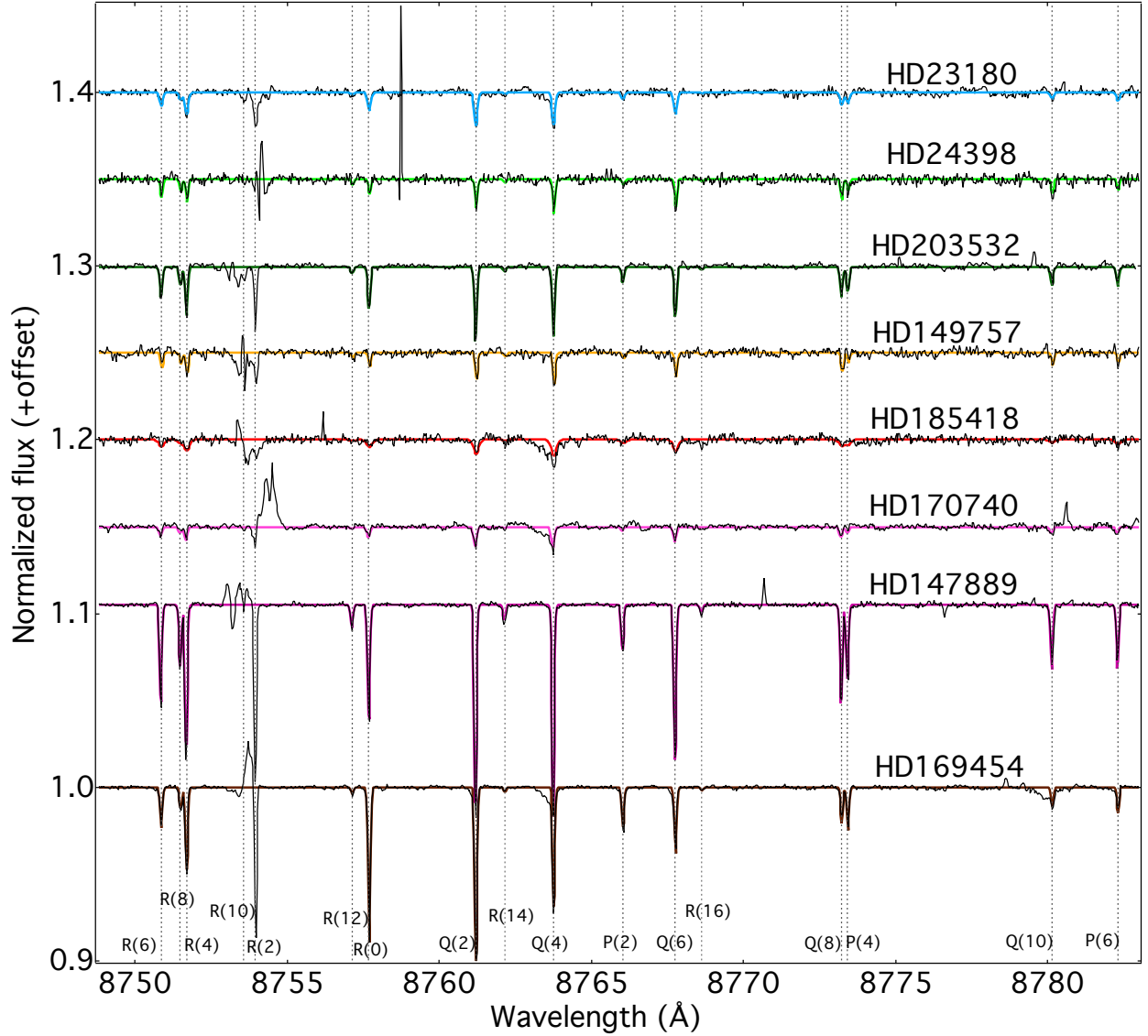
---

^{2} http://dib.uiuc.edu/c2/

Fig. 2. Observed Phillips (2–0) C_2 bands and their best-fitting model profiles. The R_{10} and R_2 lines at 8753.949 and 8753.578 Å have not been included in the fit because of the presence of a CCD artifact near these wavelengths that could not be corrected by flat-fielding. In some cases, Q(4) line is blended with a suspected DIB (or stellar line).

Table 2. Gas kinetic temperature T_{kin}, volume density n, column density N, Doppler b parameter, radial velocity v derived from Phillips (2–0) C_2 system for the selected sightlines, and C_2 column density normalized to extinction $N(C_2)/E(B–V)$.

| | | | This work | | | | Kazmierczak et al.[a] | |
Identifier	T_{kin} (k)	n (cm^{-3})	$\log N(C_2)$ (cm^{-2})	b (km s^{-1})	v (km s^{-1})	$N(C_2)/E(B–V)$	T_{02} (k)	Ref.
HD 23180	$44.7^{+5.9}_{-3.6}$	$346.5^{+68.3}_{-46.7}$	13.31 ± 0.02	1.95 ± 0.10	13.61 ± 0.06	7.3×10^{13}	20 ± 7	K09
HD 24398	$56.7^{+10.9}_{-8.4}$	$211.5^{+51.9}_{-30.2}$	13.30 ± 0.02	0.93 ± 0.13	13.97 ± 0.06	6.9×10^{13}	–	
HD 203532	$40.7^{+1.2}_{-1.3}$	$282.1^{+10.1}_{-10.2}$	13.58 ± 0.01	1.06 ± 0.04	15.40 ± 0.01	1.3×10^{14}	–	
HD 149757	$52.2^{+10.9}_{-7.9}$	$199.2^{+40.6}_{-21.1}$	13.26 ± 0.02	0.90 ± 0.15	-14.34 ± 0.06	5.6×10^{13}	42 ± 42	K10b
HD 185418	$66.8^{+6.2}_{-8.2}$	–	13.1 ± 0.1	3.55 ± 0.30	-10.73 ± 0.20	3.3×10^{13}	–	
HD 170740	$45.4^{+7.5}_{-5.8}$	$248.5^{+42.9}_{-31.1}$	13.15 ± 0.02	1.83 ± 0.11	-8.80 ± 0.07	3.1×10^{13}	14 ± 5	K10b
HD 147889	$44.1^{+0.4}_{-0.5}$	$260.7^{+3.2}_{-3.9}$	14.09 ± 0.01	0.98 ± 0.01	-7.49 ± 0.01	1.2×10^{14}	49 ± 7	K10a
HD 169454	$18.8^{+0.2}_{-0.2}$	$356.1^{+3.3}_{-2.4}$	13.85 ± 0.01	0.90 ± 0.01	-8.92 ± 0.01	7.1×10^{13}	23 ± 2	K10a

Notes. [a]Sources are K09: Kaźmierczak et al. (2009), K10a: Kaźmierczak et al. (2010a), and K10b: Kaźmierczak et al. (2010b).

Table 3. DIB equivalent widths.

DIB (Å)	23180	24398	203532	149757	185418 (mÅ)	170740	147889	169454
				C_2-DIBs				
4363	$-^a$	<0.3	4.3 ± 0.2	1.3 ± 0.4	<0.4	<0.2	11.1 ± 0.4	4.4 ± 0.2
4727^a	46.7 ± 0.9	38.3 ± 0.7	55.3 ± 1.1	17.0 ± 1.0	35.8 ± 1.0	45.3 ± 1.0	155.4 ± 2.9	95.0 ± 1.1
4734	2.3 ± 0.8	<0.5	6.5 ± 0.7	<0.6	<4	<0.5	15.2 ± 0.9	3.2 ± 0.4
4963	12.0 ± 0.8	9.6 ± 0.3	21.2 ± 0.4	3.8 ± 0.6	11.6 ± 0.7	11.2 ± 0.3	51.9 ± 0.9	24.8 ± 1.0
4969	3.8 ± 0.3	2.5 ± 0.2	2.8 ± 0.2	1.4 ± 0.5	1.5 ± 0.3	2.2 ± 0.3	9.7 ± 0.8	6.4 ± 0.3
4979	3.0 ± 0.3	2.5 ± 0.3	3.6 ± 0.3	1.3 ± 0.4	1.9 ± 0.3	2.0 ± 0.3	14.1 ± 0.9	3.9 ± 0.3
4984	6.6 ± 0.3	3.6 ± 0.3	8.2 ± 0.4	2.4 ± 0.5	4.0 ± 0.3	3.6 ± 0.2	24.4 ± 1.1	11.2 ± 0.3
5003	$-^a$	$-^a$	4.1 ± 0.2	2.6 ± 0.5	$-^a$	$-^a$	5.6 ± 0.5	$-^a$
5170	4.5 ± 0.4	1.6 ± 0.2	3.2 ± 0.5	1.3 ± 0.5	1.9 ± 0.3	1.9 ± 0.3	11.1 ± 0.8	5.3 ± 0.2
5175	2.3 ± 0.2	13.5 ± 0.4	7.9 ± 0.3	2.8 ± 0.8	2.3 ± 0.5	6.2 ± 0.5	31.7 ± 1.0	16.1 ± 0.8
5418	10.3 ± 0.4	5.1 ± 0.3	12.3 ± 0.3	3.7 ± 0.4	5.4 ± 0.4	5.1 ± 0.3	40.8 ± 0.9	16.4 ± 0.3
5512	7.5 ± 0.3	5.0 ± 0.2	10.6 ± 0.3	2.2 ± 0.4	3.8 ± 0.4	4.5 ± 0.3	18.2 ± 0.5	14.6 ± 0.3
5541	4.5 ± 0.3	2.1 ± 0.2	4.7 ± 0.2	1.4 ± 0.3	3.3 ± 0.3	1.7 ± 0.2	10.9 ± 0.8	9.3 ± 0.3
5546	4.0 ± 0.4	2.0 ± 0.3	4.7 ± 0.3	1.5 ± 0.4	1.9 ± 0.3	1.7 ± 0.1	8.2 ± 0.8	5.7 ± 0.3
5762	4.6 ± 0.3	2.7 ± 0.2	4.1 ± 0.3	2.8 ± 0.5	7.2 ± 0.5	2.3 ± 0.3	11.6 ± 1.0	8.1 ± 0.3
5769	4.8 ± 0.4	1.5 ± 0.3	5.2 ± 0.3	<2	<4.5	1.2 ± 0.2	20.6 ± 0.8	5.4 ± 0.3
5793^b	6.3 ± 0.7	5.3 ± 0.6	5.3 ± 0.4	1.7 ± 0.4	3.9 ± 0.5	3.3 ± 0.4	15.8 ± 1.0	8.7 ± 0.3
6729	4.2 ± 0.6	5.1 ± 1.5	3.5 ± 0.7	<5	<4	<4	15.5 ± 1.5	6.6 ± 1
				New C_2-DIB candidates				
4737.5	0.8 ± 0.3	<0.4	1.2 ± 0.2	<0.5	<0.5	blend^a	3.0 ± 0.7	0.5 ± 0.2
5547.4	0.7 ± 0.2	0.9 ± 0.2	0.8 ± 0.1	<0.7	1.3 ± 0.2	0.9 ± 0.1	2.5 ± 0.6	2.0 ± 0.3
5769.8	1.0 ± 0.2	0.7 ± 0.2	0.7 ± 0.2	<1.3	<1.5	0.7 ± 0.1	1.9 ± 0.7	1.8 ± 0.2
				Selected strong DIBs				
5850	31.1 ± 0.6	20.4 ± 0.7	28.0 ± 0.3	10.9 ± 0.6	27.6 ± 0.6	21.0 ± 0.4	64.6 ± 1.0	61.0 ± 0.7
5797	58.6 ± 1.0	51.4 ± 0.6	53.1 ± 1.1	28.3 ± 0.9	80.3 ± 1.2	61.2 ± 0.9	143.5 ± 2.5	158.4 ± 2.3
5780	80.0 ± 0.9	97.2 ± 0.8	108.6 ± 0.9	65.6 ± 1.3	266.1 ± 1.8	237.0 ± 1.6	346.9 ± 2.9	463.9 ± 2.2
6196	12.6 ± 0.6	13.6 ± 0.7	12.7 ± 0.6	8.5 ± 0.7	33.7 ± 2.1	23.7 ± 0.9	34.8 ± 1.6	52.4 ± 0.6
6234	5.9 ± 0.7	5.9 ± 0.5	4.7 ± 0.3	2.2 ± 1.0	9.1 ± 0.7	11.6 ± 0.4	14.4 ± 1.4	15.1 ± 1.2
6376	7.8 ± 0.6	7.7 ± 0.6	7.7 ± 0.7	5.0 ± 0.7	17.3 ± 1.2	10.4 ± 0.9	34.1 ± 2.4	20.0 ± 1.5
6379	37.6 ± 0.6	57.4 ± 0.7	43.2 ± 0.4	15.2 ± 0.7	71.5 ± 0.7	55.6 ± 0.7	82.4 ± 1.8	93.3 ± 1.4
6614	45.3 ± 0.7	60.2 ± 0.6	57.7 ± 0.6	41.4 ± 1.0	166.3 ± 0.9	120.0 ± 0.6	160.6 ± 2.1	182.6 ± 1.1

Notes. $^{(a)}$blended with stellar lines, $^{(b)}$possible telluric residuals.

Inspection of Figs. 3–7 reveals clearly that sub-structures do exist for at least 14 DIBs. The shapes look very similar to those of the strong bands in previous work which have been studied in depth and found to be compatible with rotational contours of large molecules. There are strong differences from one band to another, with two or three individual branches, depending on the band, accompanied in some cases by a broad red wing. Figure 8 summarizes the observed variety of DIB profiles.

4.2. Potential additional weak C_2-DIBs

In the course of this study we noticed three weak absorption features resembling DIBs falling at the same wavelength when spectra are shifted to the cloud frame, i.e., being very likely of interstellar origin. Figure 9 displays the spectra of the targets that show clearly these features. The relative strengths are roughly similar to those found for the other C_2-DIBs, which reinforces their identification as new DIBs. These potentially new bands are centered at 4737.5, 5547.4, and 5769.8 Å, respectively. Their weakness prevents identification of sub-structures in their profiles. Two of them are found to lie 1 Å to longer wavelength of

a strong C_2-DIB. Further measurements will help in confirming these new bands. We excluded them from the correlational studies that are discussed in Sect. 8 due to large uncertainties in their EWs. For this reason, it is not possible to ascertain their C_2-DIB nature with confidence.

5. Variability of profiles among the eighteen C_2-DIBs

The main result of this study is the appearance of sub-structures with two or three sub-peaks in at least 14 C_2-DIBs, the remaining four being too weak or too contaminated (at 5003, 5762, 5793, and 6729 Å) to draw a definite conclusion. The two and three sub-peak profile structures are consistent with partially resolved rotational PQR-type branch structures and as such hint for a molecular nature of the involved carriers. It is recognised that it is not proven that the substructures are due to rotational branches and that the shortest wavelength component is an R feature, but for ease of discussion we have chosen this interpretation and to label the components as P (located at the longest wavelengths), Q, and R (shortest wavelengths). When treating the profiles as molecular rotational
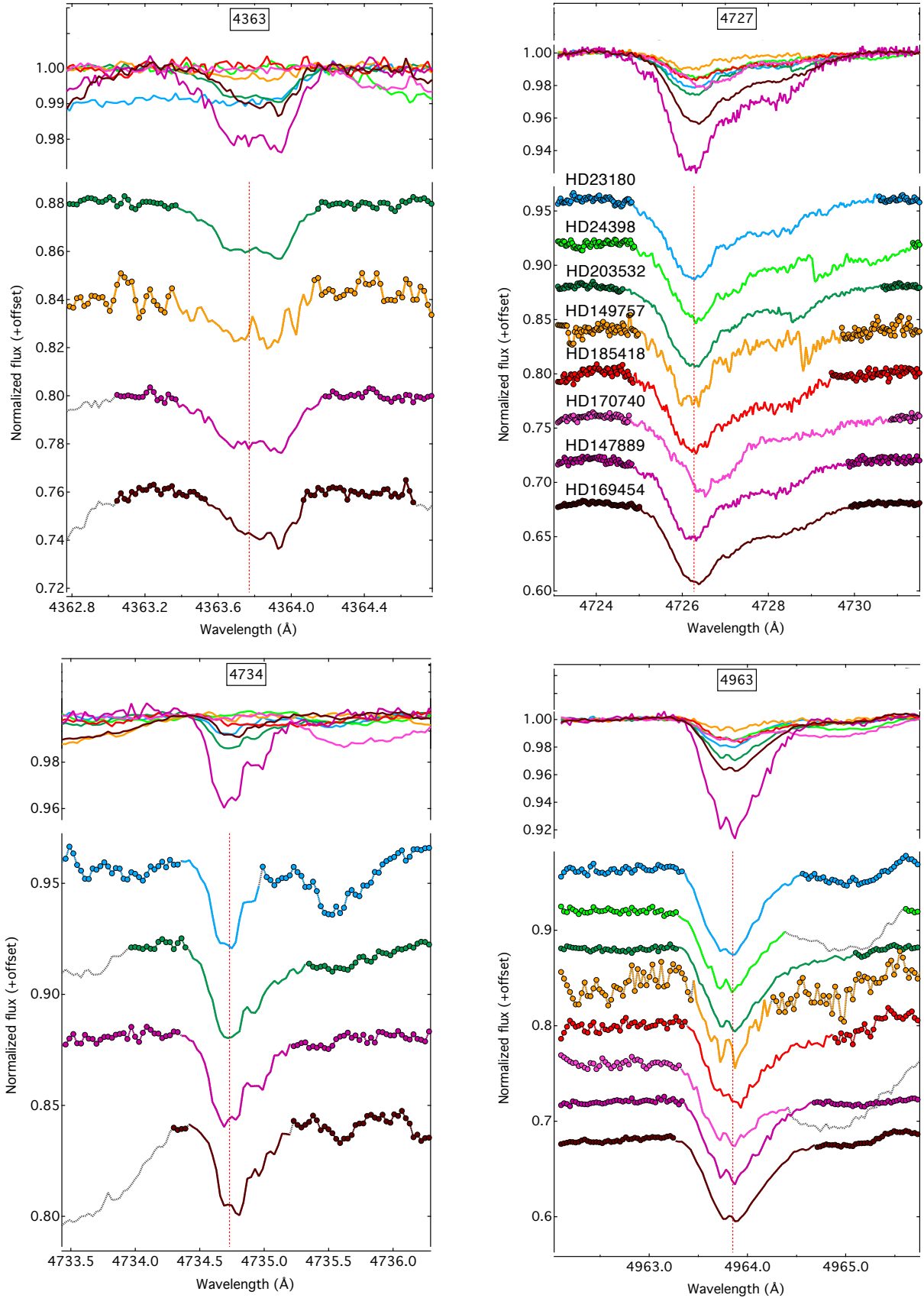
Fig. 3. The 4363, 4727, 4734, and 4963 C_2-DIBs recorded along seven single-cloud and one multi-cloud line-of-sight. *Top in all four panels*: overlaid C_2-DIB profiles at the same vertical scale for all stars. *Bottom in all four panels*: same C_2-DIB vertically displaced and depth-equalized profiles. The red dashed line shows the DIB location. See Fig. 1 for color coding.
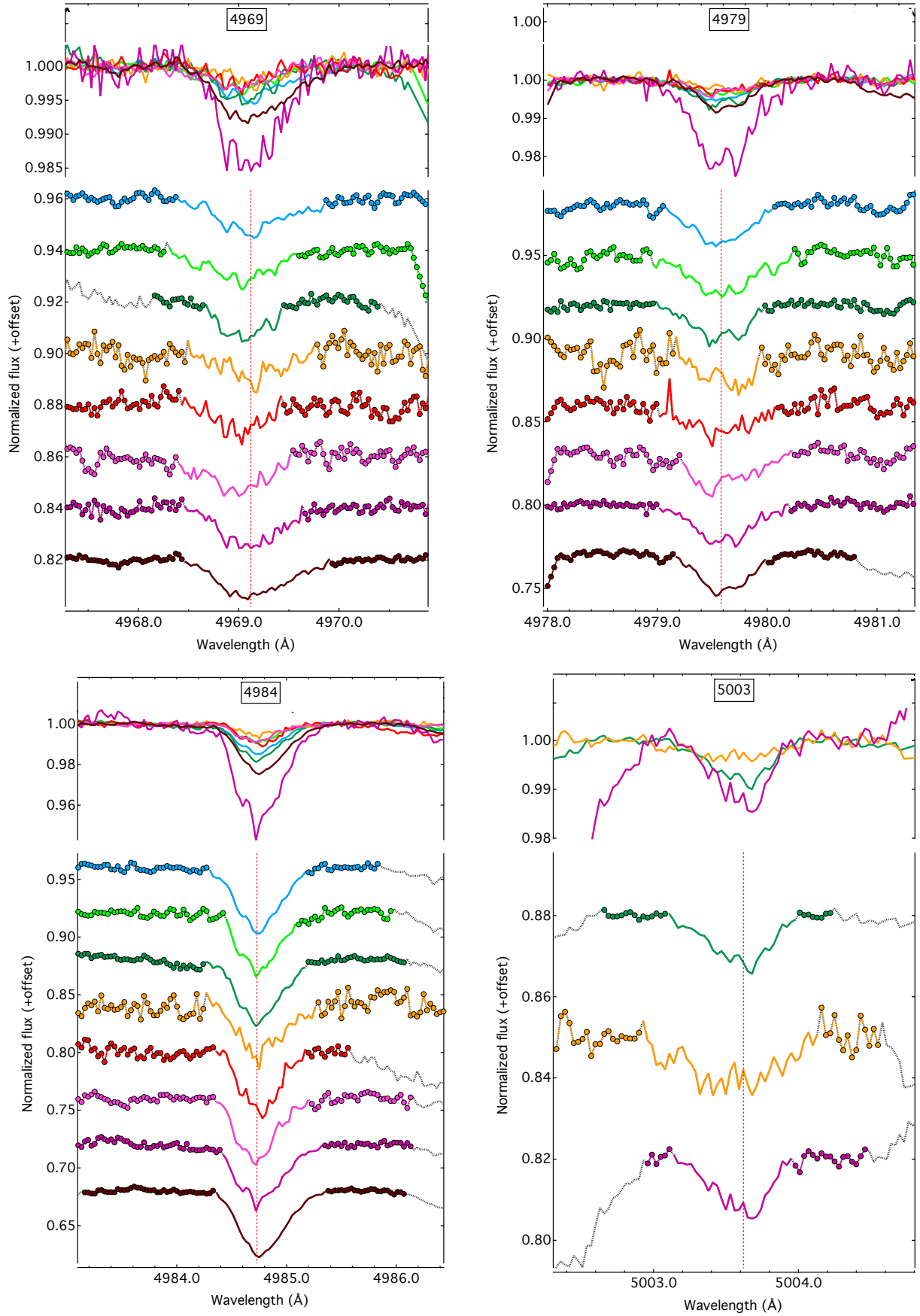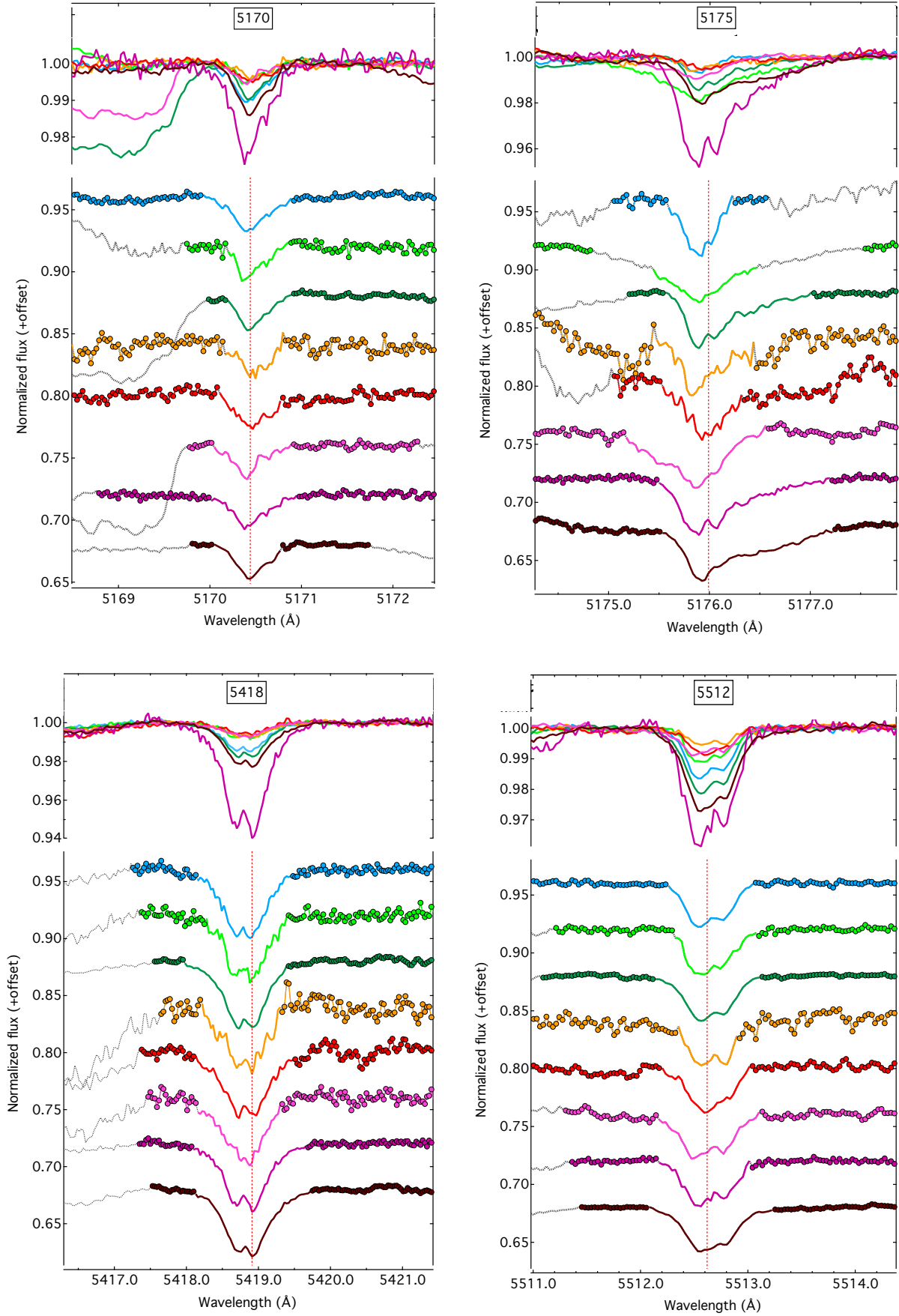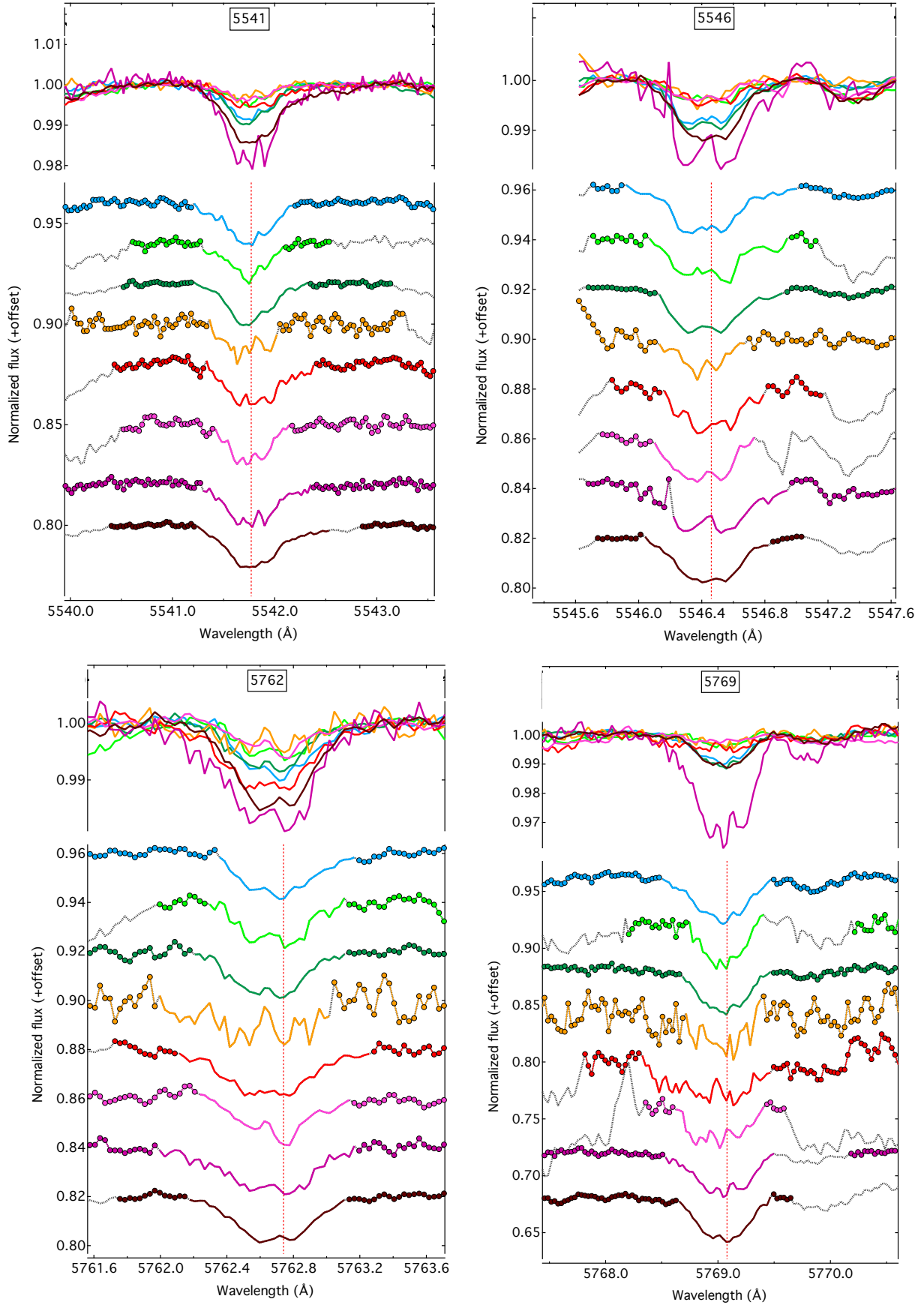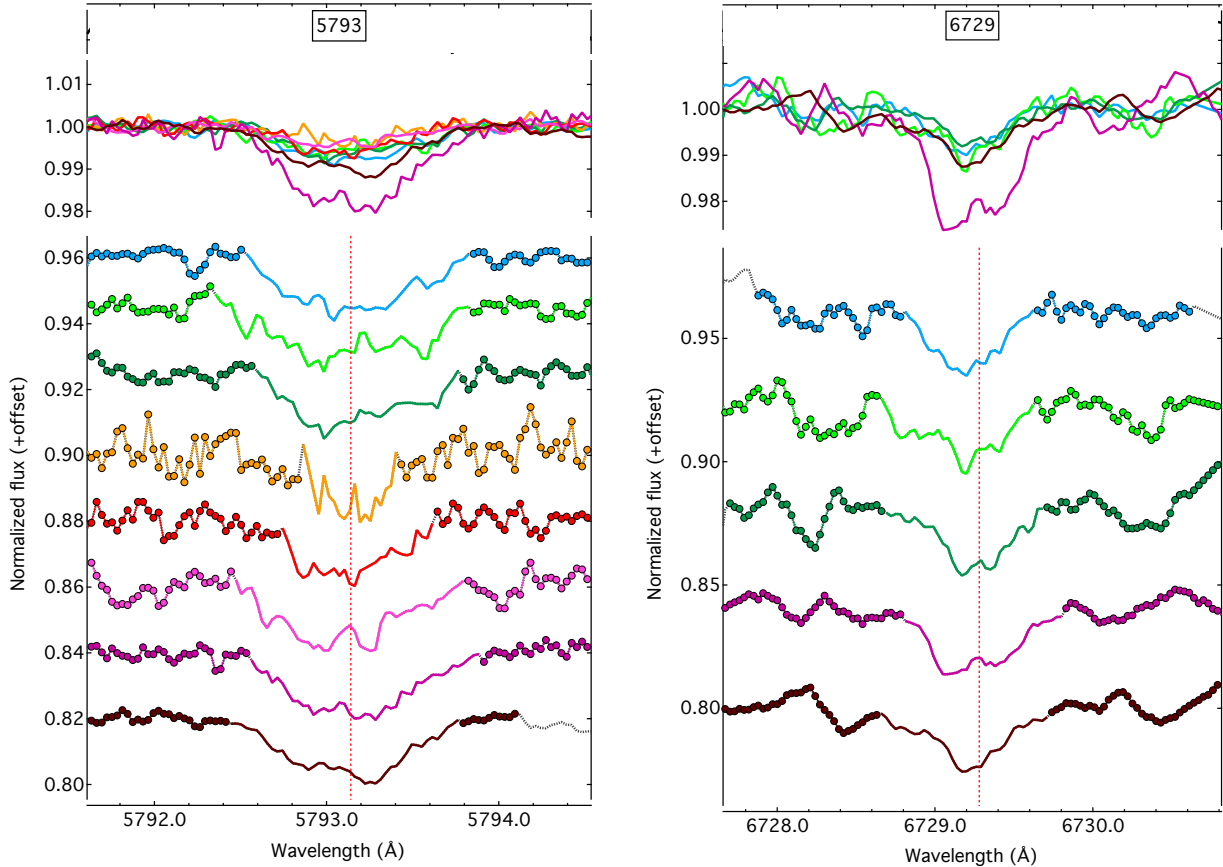
Fig. 4. The 4969, 4979, 4984, and 5003 C_2-DIBs recorded along seven single-cloud and one multi-cloud line-of-sight. *Top in all four panels*: overlaid C_2-DIB profiles at the same vertical scale for all stars. *Bottom in all four panels*: same C_2-DIB vertically displaced and depth-equalized profiles. The red dashed line shows the DIB location. See Fig. 1 for color coding. 5003 Å band is blended with stellar lines.

Fig. 5. The 5170, 5175, 5418, and 5512 C_2-DIBs recorded along seven single-cloud and one multi-cloud line-of-sight. *Top in all four panels*: overlaid C_2-DIB profiles at the same vertical scale for all stars. *Bottom in all four panels*: same C_2-DIB vertically displaced and depth-equalized profiles. The red dashed line shows the DIB location. See Fig. 1 for color coding.

Fig. 6. The 5541, 5546, 5762, and 5769 C_2-DIBs recorded along seven single-cloud and one multi-cloud line-of-sight. *Top in all four panels*: overlaid C_2-DIB profiles at the same vertical scale for all stars. *Bottom in all four panels*: same C_2-DIB vertically displaced and depth-equalized profiles. The red dashed line shows the DIB location. See Fig. 1 for color coding.

Fig. 7. The 5793 and 6729 C_2-DIBs recorded along seven single-cloud and one multi-cloud line-of-sight. *Top in all four panels*: overlaid C_2-DIB profiles at the same vertical scale for all stars. *Bottom in all four panels*: same C_2-DIB vertically displaced and depth-equalized profiles. The red dashed line shows the DIB location. See Fig. 1 for color coding.

Table 4. C_2 DIB sub-structure peak separations (cm^{-1}).

HD	4984			5418[a]			5512	5541			5546		
	$\Delta_{\nu_{PQ}}$	$\Delta_{\nu_{QR}}$	$\Delta_{\nu_{PR}}$	$\Delta_{\nu_{PR}}$	$\Delta_{\nu_{PQ}}$	$\Delta_{\nu_{QR}}$	$\Delta_{\nu_{PR}}$	$\Delta_{\nu_{PQ}}$	$\Delta_{\nu_{QR}}$	$\Delta_{\nu_{PR}}$	$\Delta_{\nu_{PQ}}$	$\Delta_{\nu_{QR}}$	$\Delta_{\nu_{PR}}$
23180	0.60	0.60	1.20	0.58	–	–	0.71	0.49	0.39	0.88	0.32	0.29	0.61
24398	0.60	0.36	0.96	0.79	–	–	0.73	0.49	0.49	0.98	0.29	0.58	0.87
203532	0.42	0.60	1.02	0.79	–	–	0.68	0.29	0.58	0.88	0.36	0.32	0.68
149757	0.83	0.81	1.64	0.62	–	–	0.74	0.39	0.65	1.04	–	–	0.39
185418	0.73	0.35	1.08	0.83	0.46	0.27	0.73	0.38	0.59	0.97	0.39	0.29	0.68
170740	0.45	0.39	0.84	0.41	0.49	0.49	0.98	0.29	0.49	0.78	–	–	0.49
147889	0.48	0.85	1.33	0.73	0.35	0.42	0.77	0.48	0.39	0.87	–	–	0.72
169454	0.48	0.36	0.84	0.52	0.31	0.49	0.80	0.49	0.29	0.78	–	–	0.49

Notes. [a]The 5418 DIB shows a two sub-peak profile structure.

contours, we assume that the upper state rotational constants are smaller than in the ground state. Selection rules can then result in different types of transitions resulting in either a two-peak profile similar to the 5797 or 6196 Å DIB profiles that then represent unresolved P and R branches or a three-peak profile that additionally displays a central Q branch. With these conventions, we have determined the peak positions of the sub-peaks (in wavenumber space; ν_P, ν_Q, and ν_R) and we have extracted the wavenumber intervals ($\Delta_{\nu_{PQ}} = \nu_Q - \nu_P$, $\Delta_{\nu_{QR}} = \nu_R - \nu_Q$ and $\Delta_{\nu_{PR}} = \nu_R - \nu_P$) between them in all relevant cases. This was done based on visual selection of regions possessing a well-defined minimum or secondary minimum, and subsequent fitting of the bottom region of each sub-structure with a second order polynomial to extract the minimum location.

The C_2-DIB sub-structure peak separations $\Delta_{\nu_{PQ}}$, $\Delta_{\nu_{QR}}$, and $\Delta_{\nu_{PR}}$ are listed in Table 4. These values are given in cm^{-1}, as this unit offer a wavelength-independent value that allows a direct comparison between the different C_2-DIBs. We did not attempt to fit the profiles with the product of individual components, as the choice of the number of components is quite subjective, especially in the case of the presence of red wings or for the weakest bands. According to the results of Table 4 and as can be seen for all DIBs in Fig. 8, the peak relative amplitudes and peak sub-structure separations are quite different among the DIBs. The separation between the P and R branch scales roughly with $B \times T$, where B is the rotational constant and T the carrier's rotational temperature (but see Huang & Oka 2015). Therefore, for the same cloud and within the assumption of the same physical
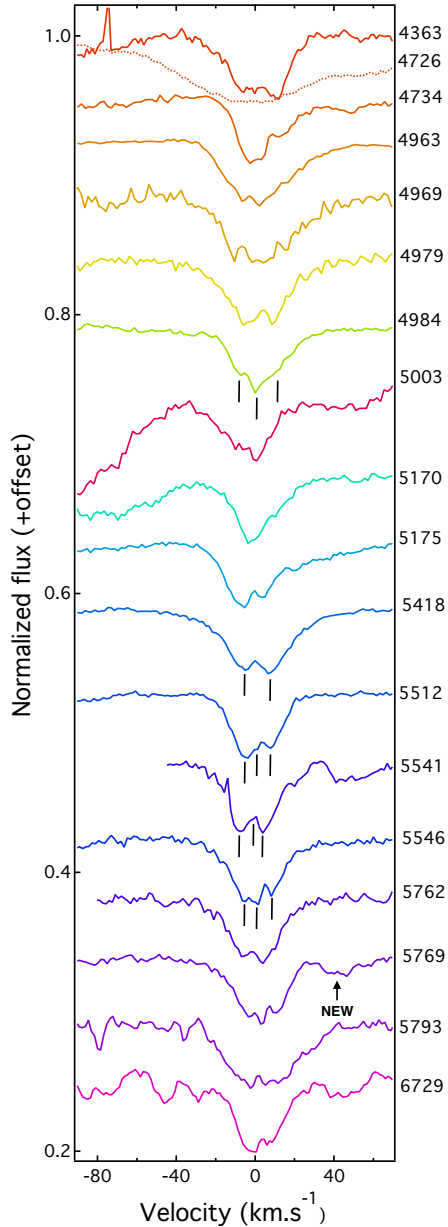
Fig. 8. Extracted average C_2-DIB profiles (i.e., from stacking profiles of HD 23180, HD 203532, and HD 147889) normalized to the same depth of 4963 Å DIB. Tick marks refer to the location of sub-peaks of Table 4.

conditions, this observed variability implies that the sizes of the carriers for the different C_2-DIBs are most likely quite different.

6. Prominent sub-structures and average spectral profiles

The generally low signal strengths do not allow clear identifications of sub-structures for all combinations of DIBs and targets. A classical method used to increase the S/N and enhance weak features is the co-addition of profiles. Some caution is needed here since different sightlines may correspond to different shapes of the same DIB, in this case co-adding sub-structures is not physical. This could be the case if the carrier internal population distributions were markedly different from one sightline to another in response to different excitations. Indeed,

such peak-to-peak variations have been observed and used to place constraints on the rotational excitation temperatures of the 6614 and 6196 Å DIB carriers (Cami et al. 2004; Kaźmierczak et al. 2009). In order to test the co-addition feasibility, we have used the sub-peak intervals of Table 4 to estimate upper limits on the profile variability. We discarded all cases for which peak determinations were too uncertain, which resulted in the selection of only five bands. For each type of interval, we normalized it by simply dividing by the mean value of the sub-peak intervals over all eight targets. Figure 10 displays the resulting normalized intervals between the sub-peaks, here as a function of the kinetic temperature $T_{\rm kin}$ for the corresponding target, derived from the C_2 analysis. Figure 10 shows that the variations from one sightline to the other for the same band are significantly smaller than the dispersion among the normalized intervals of the various DIBs for the same target, although a weak increase with temperature is discernible. It is difficult to draw firm conclusions from this, given the uncertainties in our sub-peak wavelengths. Three stars, namely, HD 23180, HD 203532, and HD 147889 have the deepest absorption bands and are characterized by a good S/N, thus have relatively clear sub-structures. Figure 10 confirms that for these three targets (marked by arrows) the sub-peak interval variability is the smallest. For this reason, we performed a co-addition of the profiles over these three targets only. Before the co-addition, the normalized DIB profiles were shifted to a common interstellar rest frame and elevated at a power in such a way that their depths are the same for the three targets. The average profiles are displayed in Fig. 8. Although they can not be considered as pure intrinsic profiles (as stated above, rotational contours may change from one target to the other), these average profiles are free from telluric or stellar contamination and we believe they are our most accurate representation of each DIB structure. Such information complements well that contained in the series of individual measurements. On the other hand, it is often difficult to preclude profile variation and for this reason we discuss the DIBs towards each of the three selected stars separately in the next section.

7. Search for profile variability among the sightlines

With the goal of going one step further in the validation of the average profiles, we investigated the potential variations of DIB profiles for the three selected single-cloud targets. In particular, measurements of the C_2 molecule rotational temperatures T_{02} defined as the average excitation temperature of the two (resp. three and four) lowest rotational levels of the ground electronic state have been performed by Kaźmierczak et al. (2009, 2010a) for two of these single-cloud sightlines. The temperatures are different: $T_{02} = 20$ K for HD 23180 and 49 K for HD 147889.

Figures 11–13 show the 18 C_2-DIB profiles for the three EDIBLES targets after normalization to reach the same maximum depth. We also show the normalized profiles for the multi-cloud target HD 169454. It is interesting to disentangle the effects of Doppler broadening due to cloud multiplicity and broadening due to increase of the excitation temperature. Coincidentally, $T_{02} = 23$ K for HD 169454, is very similar to the value measured for HD 23180. Moreover, profiles of the 6196 Å DIB have been investigated for this star as well as for HD 147889 and HD 23180 by Kaźmierczak et al. (2009). In order to better visualize differences, we show the profiles that correspond to HD 147889 superimposed on the three others because for
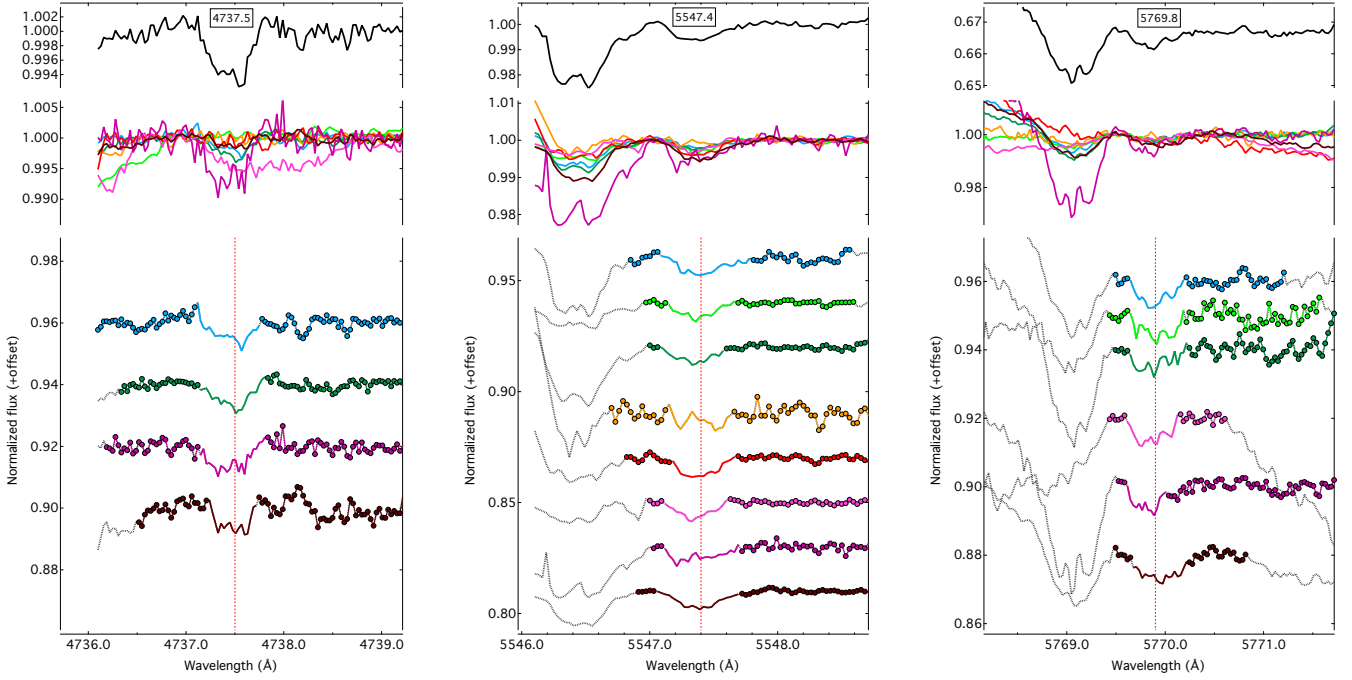
Fig. 9. Potential new detection of weak C$_2$-DIBs at 4737.5, 5547.4, and 5769.8 Å (they appear toward sigthlines where the other C$_2$-DIBs are well-detected). The red dashed line shows the DIB location. *Top graphs (black) in all three panels*: extracted average normalized profile of C2-DIBs created from stacking three single-cloud targets: HD 23180, HD 203532, and HD 147889, shown below. *Middle in all three panels*: overlaid C$_2$-DIB profiles at the same vertical scale for all stars. *Bottom in all three panels*: same C$_2$-DIB vertically displaced and depth-equalized profiles. The red dashed line shows the DIB location. The wavelengths are in the interstellar rest frame. See Fig. 1 for color coding.
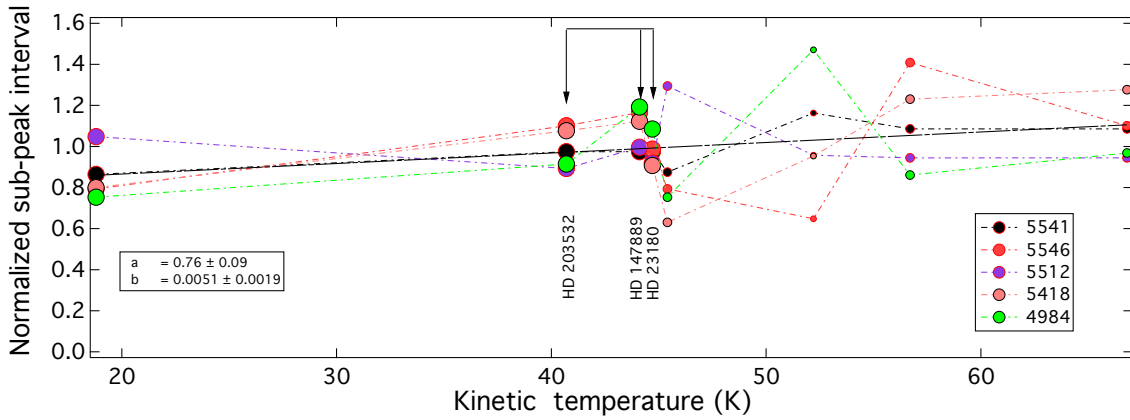
Fig. 10. Normalized spectral intervals between the sub-peaks in the profiles of several C$_2$-DIBs as a function of the C$_2$-based kinetic temperature (see text) of each target. Uncertainties on the intervals can be deduced visually from the drawn profiles in Figs. 3–7, and are on the order of the data point dispersion. The dashed line is a linear fit to the average over the five different DIBs. The size of the marker indicates the reliability of the sub-peak interval determination, again visually determined from the quoted figures. The three targets used for the co-addition of the DIB profiles are marked by arrows.

this sightline the sub-structures are the most prominent. After careful inspection of all comparison figures, we identified three categories of DIBs.

The first category corresponds to the existence of sub-structures for the four targets, and no detected variation in the total width of the band nor in the locations of the sub-peaks. Falling in this category are DIBs 4727, 4734, 4963, 4984, 5418, 5512, and 5541 Å (Fig. 11) confirming an earlier result by Galazutdinov et al. (2008) for the 4963, 5418, and 5512 Å DIBs. Therefore, for those bands the stacking is justified as a means to enhance the profile structures. It is worth noting that for 4984, 5512, and 5541 Å DIBs the sub-structures are smoother in the case of lower temperatures.

The second category corresponds to the weakest bands for which individual profiles do not clearly reveal sub-structures well above the noise and no apparent variations of the total width. In those cases, the co-addition is justified since it simply improves the S/N. This is the case for the 4969, 4979, 5003 and 5170 DIBs (Fig. 12). In the case of the 5762 and 5793 Å DIBs, the co-addition does not bring any improvement. We believe this may be due to the effect of telluric residuals (see the remark on the HITRAN database in Sect. 2.1) that become very important for targets with the weakest absorbing column. Note that these are the two weakest of all C$_2$-bands. Further measurements and improved telluric corrections are needed to confirm their sub-peaks.
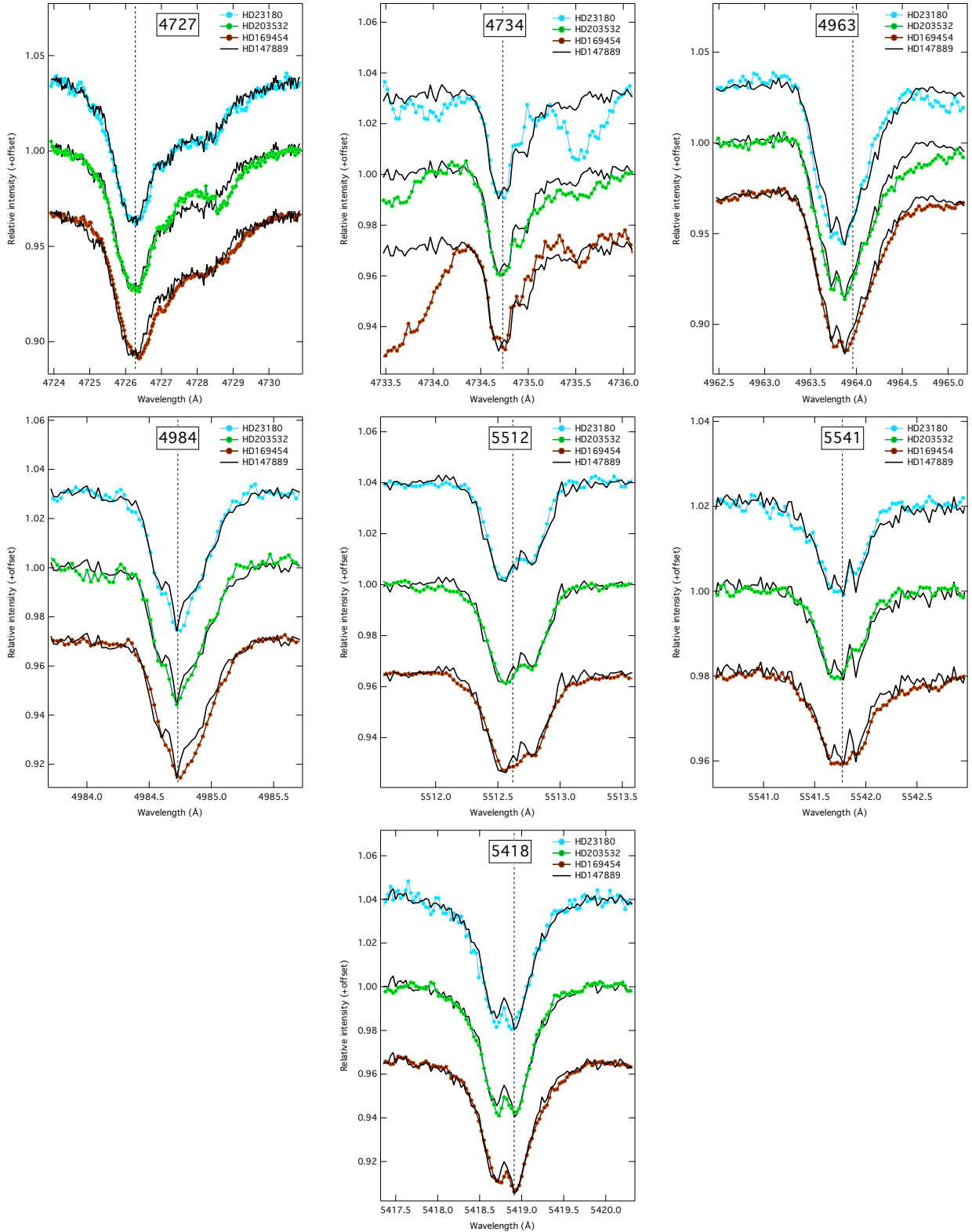
Fig. 11. Comparison between C$_2$ DIB profiles normalized to their central depths toward HD 23180 (blue), HD 203532 (green), HD 147889 (black), and HD 169454 (brown). The first three targets are those chosen for profile co-additions, for which results are shown in previous figures. The C$_2$ excitation temperatures are 20, 23, and 49 K for HD 23180, HD 169454, and HD 147889, respectively (see Table 2).

The third DIB category corresponds to the detection of profile variations among the four targets, and this may potentially reveal a response to the excitation temperature. Indeed, the full DIB width appears smaller for HD 23180 (T_{02} = 20 K) and, to a lesser extent, for HD 203532 (unmeasured T_{02}) compared to HD 147889 (T_{02} = 49 K). Interestingly, these DIBs are also narrower for the multi-cloud star HD 169454 (T_{02} = 23 K) than for HD 147889, an effect opposite to the expected broadening due to cloud multiplicity. Moreover, the amplitudes of the sub-peaks appear smaller for HD 23180,
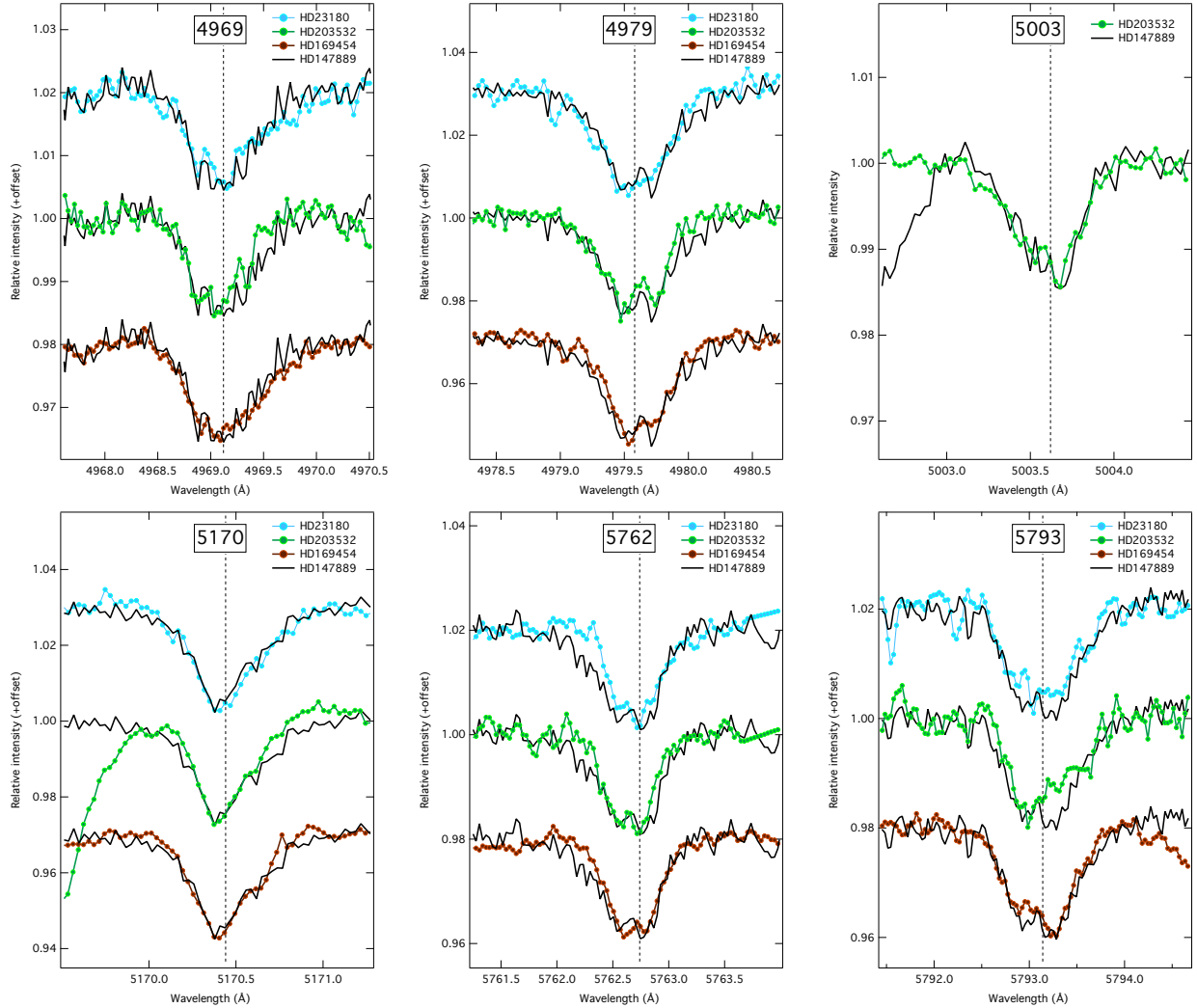
Fig. 12. Same as Fig. 11 but for 4969, 4979, 5003, 5170, 5762, and 5793 Å.

HD 203532 and HD 169454 compared to HD 147889. Falling in this category are the 4363, 5541, and 5769 Å DIBs. Identical, but less clearly measured effects can also be seen for DIBs 5175, 5546, and 6729 Å. If these simultaneous variations in width and peak amplitudes are actually linked to the variation of the rotational excitation, then for these DIBs the average profile does not correspond to any intrinsic profile. However, we have kept these average profiles in Fig. 8. Interestingly, the DIBs from this third category are all very tightly correlated with the C_2 column, as discussed in the next section.

8. Correlational studies

8.1. Correlations with the C_2 column

Our combined measurements of C_2 columns and weak DIB equivalent widths towards single-cloud targets constitute an ideal dataset for the study of any link between the C_2 molecule and each DIB carrier. Figure 14 displays the equivalent widths of the recorded C_2-DIBs as a function of the C_2 column density $N(C_2)$. We have superimposed on each figure the corresponding previous measurements from Galazutdinov et al. (2006). We did not include the 5003 Å band which was not studied by Galazutdinov et al. (2006) and for which we have only three valid data points due to heavy stellar contamination. It can be seen

that all our data points fall within the set of points from these authors, revealing good agreement with all these measurements. On the other hand, it can be seen that the correlation with $N(C_2)$ is significantly tighter in the case of our targets. We interpret this as a consequence of our accurate determination of $N(C_2)$, the excellent S/N of EDIBLES spectra, our careful selection of mono-cloud sightlines and correction for telluric and stellar features. Note that we have also included the multi-cloud sightline HD 169454 in these figures. The corresponding data point always falls within the Galazutdinov et al. (2006) set of points. However, for many DIBs it is the most discrepant point if one considers our results only. This is a strong indication that the C_2-DIBs are very well correlated with the C_2 molecule, and that a large fraction of the dispersion around the linear relationship is due to cloud multiplicity.

8.2. Respective influence of C_2 column and reddening

The existence of a good correlation with $N(C_2)$ is not a sufficient condition for qualification as C_2-DIB and this has been discussed in detail by Galazutdinov et al. (2006) and Kaźmierczak et al. (2014). One way to establish this qualification is to compare the dependencies of the measured EWs on both the C_2 column and another parameter representing the quantity of interstellar matter, e.g., the reddening or the gas column. A C_2-DIB is one that is
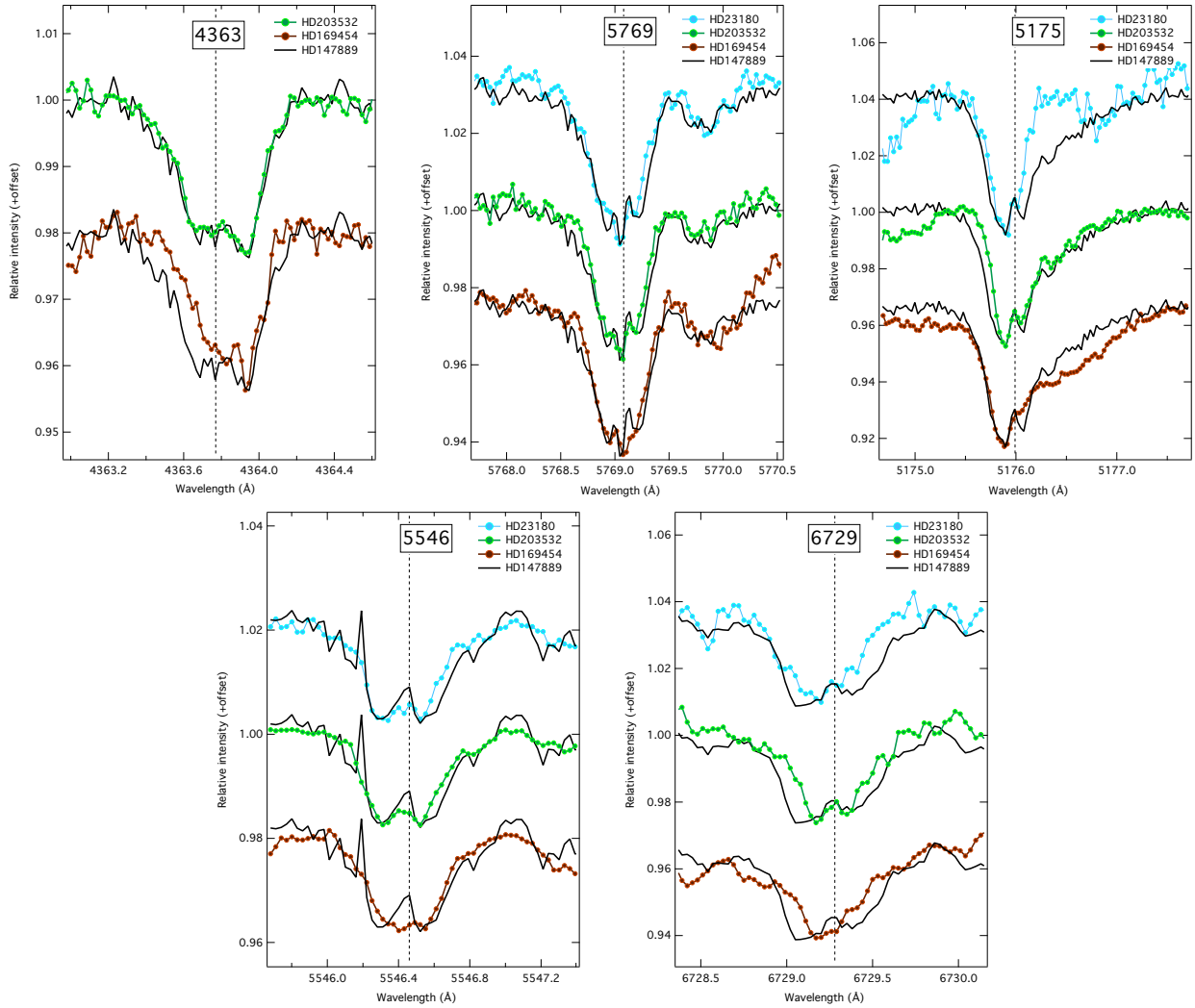
Fig. 13. Same as Fig. 11 but for 4363, 5769, 5175, 5546, and 6729 Å.

more tightly correlated with $N(C_2)$ than with these other parameters. Inspired by the study of Ensor et al. (2017), we have used our new EDIBLES dataset of C_2 and non-C_2 DIBs to perform a simplified parametric analysis restricted to the reddening and $N(C_2)$.

For each DIB we performed a linear regression between the DIB EWs and both $E(B-V)$ and the column $N(C_2)$:

$$EW = a \times N(C_2) + b \times E(B-V), \qquad (1)$$

We took into account uncertainties on EWs but assumed $E(B-V)$ and $N(C_2)$ are known with accuracy. We then computed $A = a/\sigma(a)$ and $B = b/\sigma(b)$, $\sigma(a)$, and $\sigma(b)$ being the standard deviations found from the adjustment for the partial derivatives a and b. Since $E(B-V)$ and $N(C_2)$ are assumed to be accurately defined, the dimensionless quantities A and B represent the tightness of the links between the DIB and each of the two variables $E(B-V)$ and $N(C_2)$. We then normalized the vector A, B in the system of reference $N(C_2)$ and $E(B-V)$ by dividing A and B by $\sqrt{(A^2 + B^2)}$.

Figure 15 is a representation of the corresponding "vectors". The orientation of each vector points to the parameter that governs the DIB strength (for vectors oriented vertically or horizontally) or, in intermediate cases, represents their respective

influence. Note that we performed the regression with and without inclusion of HD 169454 (the multi-cloud target) and of the highly reddened HD 147889 to test their influence. We find that the regression results do not change significantly except for the weak 6729 Å band that has clearly the most contaminated spectrum (see Fig. 7). We removed this DIB from the regression and show the results that were obtained using all targets.

Figure 15 reveals a gap between two series of DIBs. The first series corresponds to strong positive correlation with $N(C_2)$ and weak or even negative correlation with $E(B-V)$. The list of bands from this series is in total agreement with the 17 C_2-DIBs reported by Thorburn et al. (2003) in their Table 4.a as their main C_2-DIBs. In terms of relative correlation with C_2, the rankings of all six C_2-DIBs which are common to the two studies indeed agree to within the stated uncertainties. Moreover, our most tightly correlated 4734 and 5769 Å bands are also those noticed by these authors as their main C_2-DIBs. Remarkably, the $E(B-V)$ correlation coefficient for those two bands is found to be negative. The second series corresponds to the strong DIBs that follow the reddening $E(B-V)$ rather than C_2. At the margin of the C_2-DIBs group is the particular 5850 Å DIB. Interestingly, it has been classified as non-C_2 DIB (Kaźmierczak et al. 2010b) and as C_2-DIB (Kaźmierczak et al. 2014) in subsequent analyses. This band is definitely peculiar and deserves further study. Finally, we
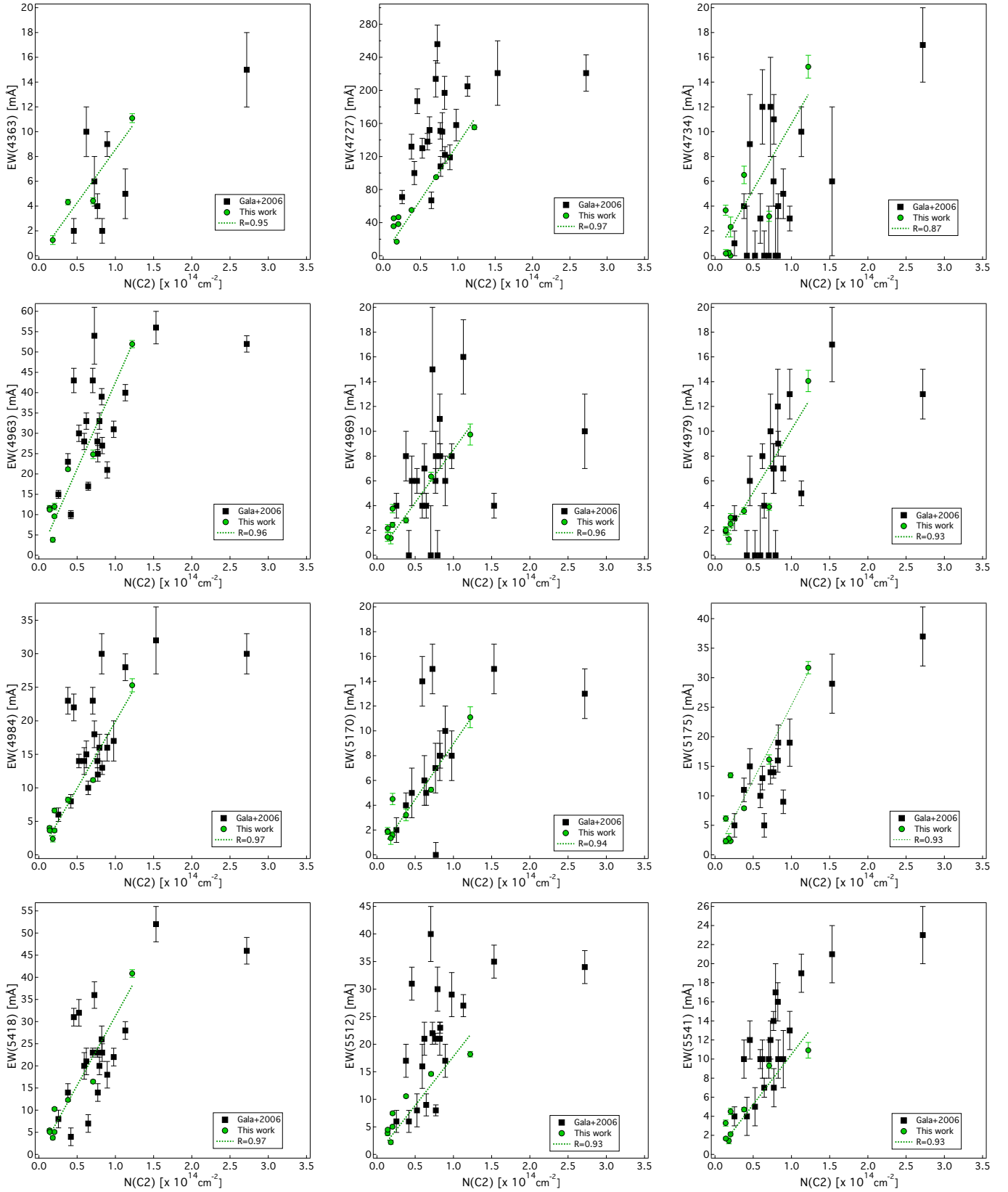
Fig. 14. Correlations between the DIB equivalent widths and the C_2 column (green filled circles). Superimposed as black squares are the results of Galazutdinov et al. (2006). R is the Pearson coefficient for our data only. The multi-cloud target HD 169454 value corresponds to $N(C_2) = 0.71 \times 10^{14}$ cm^{-2}.
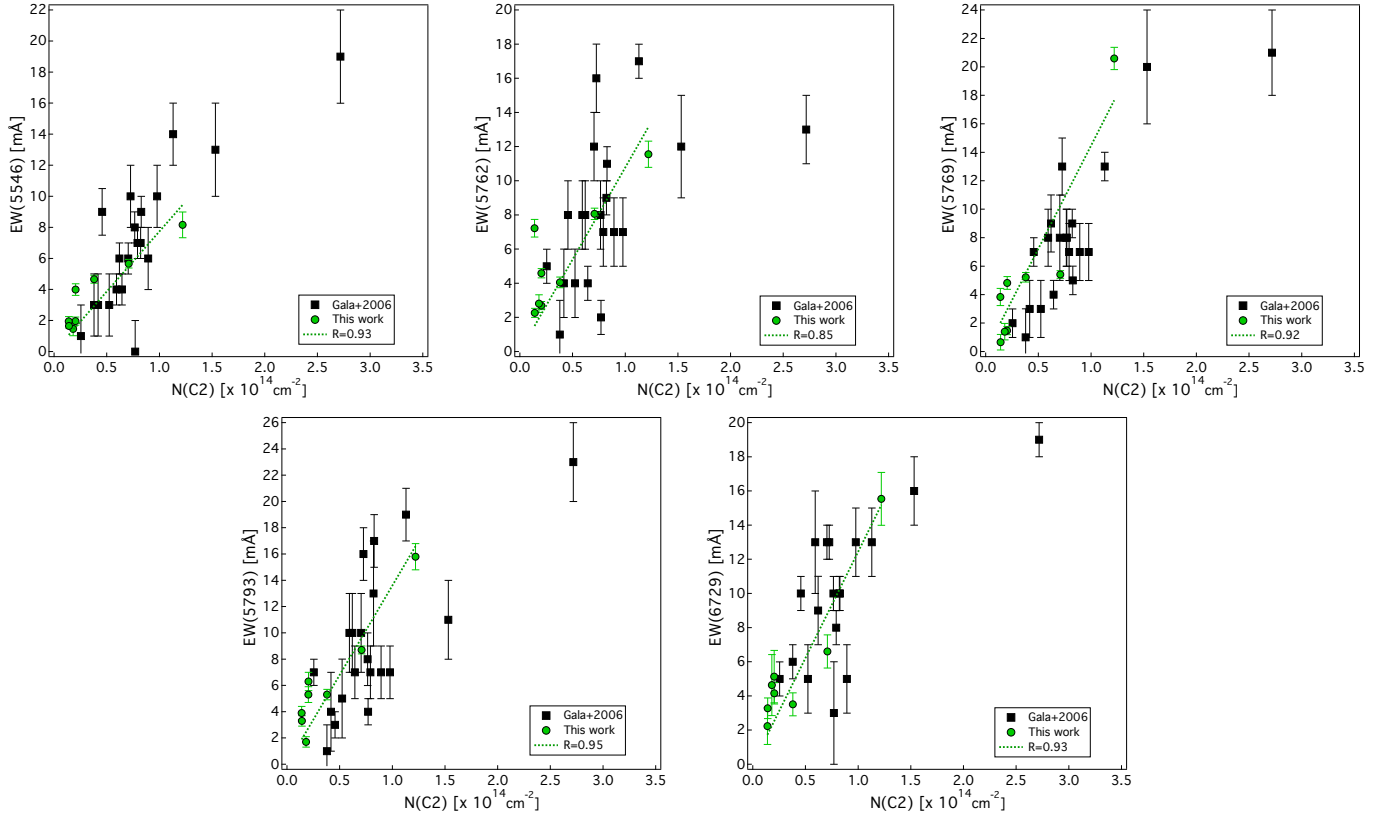
Fig. 14 . continued.

note that 4727 and 5762 Å DIBs seem to be similarly correlated to $E(B–V)$ and $N(C_2)$.

9. Summary and conclusion

We have used the high-quality spectra of the EDIBLES survey to select those sightlines that are characterized by both a high C_2 column and a single Doppler component of interstellar absorption (the single-cloud criterion). To achieve the selection, EDIBLES spectra were corrected for atmospheric lines, exposures of the same target were combined and the spectral intervals co-added to form a unique spectrum. The C_2 selection was based on the detection of the C_2 (2–0) (8750–8849 Å) Phillips system and the single-cloud selection was based on profile-fitting of the Na I UV and optical doublets. Seven targets were selected and studied together with one multi-cloud sightline.

The C_2 Phillips bands were fitted to extract the C_2 column, radial velocity and kinetic temperature as well as the gas volume density for each sightline. The absorption bands of the 18 (Thorburn et al. 2003) C_2-DIBs were extracted. Their equivalent widths as well as the EWs of eight strong DIBs were measured and are provided with their measurement uncertainties. Three additional C_2-DIB candidates were detected. The C_2-DIB EWs were compared with the reddening and the C_2 column by means of a linear regression on both quantities. Two categories of DIBs were derived, with a significant gap between the two. The first category corresponds to those classified as C_2-DIBs by Thorburn et al. (2003) and the second to the strong DIBs more tightly correlated with the reddening. A particular case is the 5850 Å band which seems to belong to a different family. In the case of the C_2-DIBs, their EWs are found to be very tightly correlated with C_2 column densities. We interpret this as

a consequence of accurate $N(C_2)$, high S/N, a careful selection of mono-cloud sightlines and correction for telluric and stellar features.

Individual profiles are presented for all targets and DIBs. We also co-added the DIB profiles of three different sightlines to enhance the sub-structures. The main result of this study is the presence of sub-structures with two or three sub-peaks in at least 14 DIBs, the remaining two being too weak to draw a definite conclusion. The two and three sub-peak profile structures are consistent with unresolved rotational branch structures of a molecular carrier. The two sub-peak profiles are very similar to those of the strong 6196 or 5797 Å DIBs, while the three sub-peak profiles are very similar to the one of the strong 6614 Å DIB. The profiles of the 18 C_2 DIBs were studied as a function of the transition and as a function of the sightline:

– Profile variability among the C_2-DIBs for the same sightline: the differences in peak relative amplitudes and peak substructure separations found among the 18 C_2 bands suggest that they correspond to different molecular carriers or electronic transition symmetries, and factors governing the level populations.

– Profile variability among the targets for the same C_2-DIB: three C_2-DIB categories were derived. Several C_2-DIBs appear to keep identical profiles among targets characterized by different C_2 rotational temperatures, however, for others, there is a potential detection of a response to the temperature, namely, a global broadening of the absorption band and slightly larger separations between the internal sub-structures at higher temperature. Such effects are similar to those detected for the 6614 Å band by Cami et al. (2004) and for the 6196 Å band by Kaźmierczak et al. (2009), and are likely associated with shifting Boltzmann maxima of
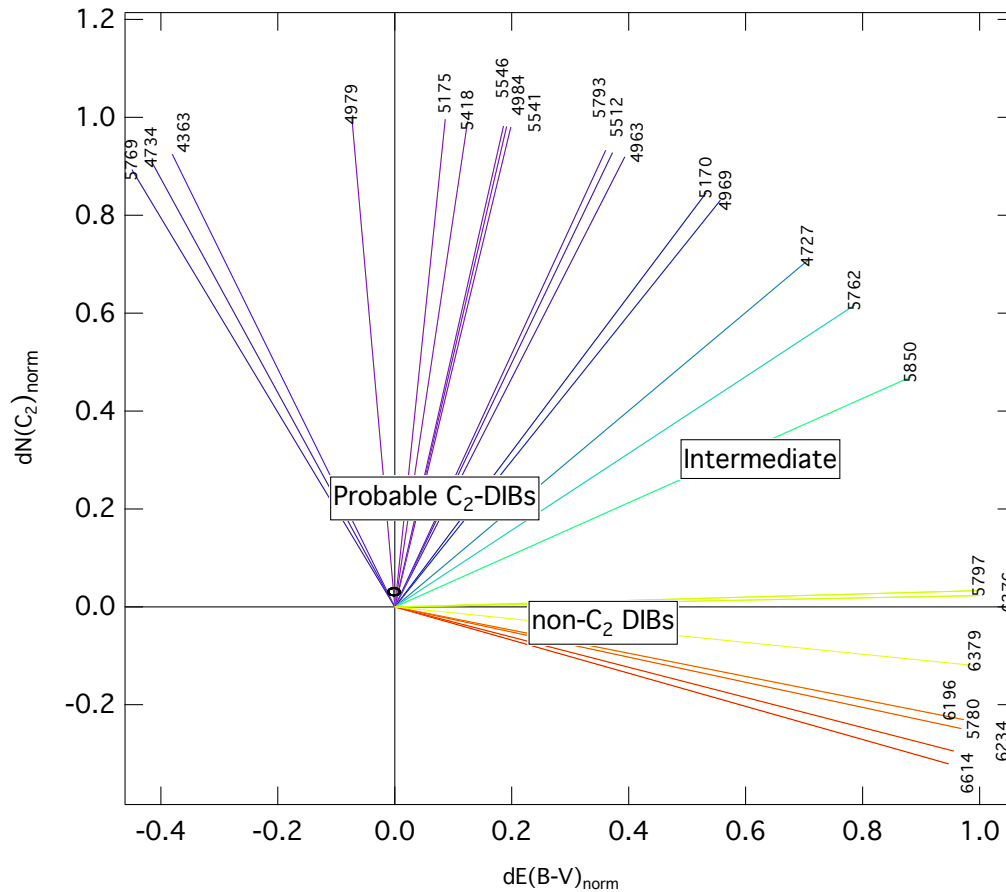
Fig. 15. Decomposition of the C_2 and reddening influence.

rotational branches of the molecular carrier. Finally, for a fraction of the DIBs, the variability (or absence of variability) could not be assessed due to their weakness.

References

Bacalla, X. L., Linnartz, H., Cox, N. L. J., et al. 2018, A&A, submitted
Bertaux, J. L., Lallement, R., Ferron, S., Boonne, C., & Bodichon, R. 2014, A&A, 564, A46
Cami, J., Salama, F., Jiménez-Vicente, J., Galazutdinov, G. A., & Krełowski, J. 2004, ApJ, 611, L113
Campbell, E. K., Holz, M., Gerlich, D., & Maier, J. P. 2015, Nature, 523, 322
Cordiner, M. A., Cox, N. L. J., Lallement, R., et al. 2017, ApJ, 843, L2
Cox, N. L. J., Cami, J., Farhang, A., et al. 2017, A&A, 606, A76
Ehrenfreund, P., & Foing, B. H. 1996, A&A, 307, L25
Ensor, T., Cami, J., Bhatt, N. H., & Soddu, A. 2017, ApJ, 836, 162
Galazutdinov, G., Stachowska, W., Musaev, F., et al. 2002, A&A, 396, 987
Galazutdinov, G. A., Gnaciński, P., Han, I., et al. 2006, A&A, 447, 589
Galazutdinov, G. A., LoCurto, G., & Krełowski, J. 2008, ApJ, 682, 1076
Gordon, I. E., Rothman, L. S., Hill, C., et al. 2017, J. Quant. Spectr. Rad. Transf., 203, 3
Huang, J., & Oka, T. 2015, Mol. Phys., 113, 2159
Jenkins, E. B. 2009, ApJ, 700, 1299

Kaźmierczak, M., Gnaciński, P., Schmidt, M. R., et al. 2009, A&A, 498, 785
Kaźmierczak, M., Schmidt, M. R., Bondar, A., & Krełowski, J. 2010a, MNRAS, 402, 2548
Kaźmierczak, M., Schmidt, M. R., Galazutdinov, G. A., et al. 2010b, MNRAS, 408, 1590
Kaźmierczak, M., Schmidt, M., Weselak, T., Galazutdinov, G., & Krełowski, J. 2014, in The Diffuse Interstellar Bands, eds. J. Cami, & N. L. J. Cox, IAU Symp., 297, 121
Krełowski, J., & Schmidt, M. 1997, ApJ, 477, 209
Lallement, R., Cox, N. L. J., Cami, J., et al. 2018, A&A, 614, A28
Lan, T.-W., Ménard, B., & Zhu, G. 2015, MNRAS, 452, 3629
Puspitarini, L., & Lallement, R. 2012, A&A, 545, A21
Sarre, P. J. 2006, J. Mol. Spect., 238, 1
Sarre, P. J., Miles, J. R., Kerr, T. H., et al. 1995, MNRAS, 277, L41
Schmidt, M. R., Krełowski, J., Galazutdinov, G. A., et al. 2014, MNRAS, 441, 1134
Słyk, K., Galazutdinov, G. A., Musaev, F. A., et al. 2006, A&A, 448, 221
Snow, T. P., & McCall, B. J. 2006, ARA&A, 44, 367
Sonnentrucker, P., Welty, D. E., Thorburn, J. A., & York, D. G. 2007, ApJS, 168, 58
Spieler, S., Kuhn, M., Postler, J., et al. 2017, ApJ, 846, 168
Thorburn, J. A., Hobbs, L. M., McCall, B. J., et al. 2003, ApJ, 584, 339
Valencic, L. A., Clayton, G. C., & Gordon, K. D. 2004, ApJ, 616, 912
van Dishoeck, E. F., & Black, J. H. 1982, ApJ, 258, 533
Vos, D. A. I., Cox, N. L. J., Kaper, L., Spaans, M., & Ehrenfreund, P. 2011, A&A, 533, A129
Walker, G. A. H., Webster, A. S., Bohlender, D. A., & Krełowski, J. 2001, ApJ, 561, 272
Walker, G. A. H., Campbell, E. K., Maier, J. P., & Bohlender, D. 2017, ApJ, 843, 56
Wegner, W. 2003, Astron. Nachr., 324, 219
Welty, D. E., & Hobbs, L. M. 2001, ApJS, 133, 345